Solid Earth, 11, 2303–2325, 2020
https://doi.org/10.5194/se-11-2303-2020

Solid Earth Open Access EGU

Unraveling the origins and P-T-t evolution of the allochthonous Sobrado unit (Órdenes Complex, NW Spain) using combined U–Pb titanite, monazite and zircon geochronology and rare-earth element (REE) geochemistry

José Manuel Benítez-Pérez[1,3], Pedro Castiñeiras[2], Juan Gómez-Barreiro[3], José R. Martínez Catalán[3], Andrew Kylander-Clark[4], and Robert Holdsworth[5]

[1]Centro de Ciências e Tecnologias Nucleares, Instituto Superior Técnico, Universidad de Lisboa, Estrada Nacional 10 (km 139,7), 2695-066, Bobadela, Portugal
[2]Departamento de Mineralogía y Petrología, Facultad de Ciencias Geológicas, Universidad Complutense de Madrid, C/José Antonio Novais, 12, Ciudad Universitaria, 28040, Madrid, Spain
[3]Departamento de Geología, Universidad de Salamanca, Pza. de los Caídos s/n, 37008, Salamanca, Spain
[4]Department of Earth Science, University of California, Santa Barbara, CA 93106, USA
[5]Earth Science Department, Durham University, Science Labs, Durham DH1 3LE, UK

Correspondence: Juan Gómez Barreiro (jugb@usal.es)

Received: 19 March 2020 – Discussion started: 20 April 2020
Revised: 29 September 2020 – Accepted: 2 October 2020 – Published: 30 November 2020

Abstract. The Sobrado unit, within the upper part of the Órdenes Complex (NW Spain) represents an allochthonous tectonic slice of exhumed high-grade metamorphic rocks formed during a complex sequence of orogenic processes in the middle to lower crust. In order to constrain those processes, U–Pb geochronology and rare-earth element (REE) analyses of accessory minerals in migmatitic paragneiss (monazite, zircon) and mylonitic amphibolites (titanite) were conducted using laser ablation split stream inductively coupled plasma mass spectrometry (LASS-ICP-MS). The youngest metamorphic zircon age obtained coincides with a Middle Devonian concordia monazite age (∼ 380 Ma) and is interpreted to represent the minimum age of the Sobrado high-P granulite facies metamorphism that occurred during the early stages of the Variscan orogeny. Metamorphic titanite from the mylonitic amphibolites yield a Late Devonian age (∼ 365 Ma) and track the progressive exhumation of the Sobrado unit. In zircon, cathodoluminescence images and REE analyses allow two aliquots with different origins in the paragneiss to be distinguished. An Early Ordovician age (∼ 490 Ma) was obtained for metamorphic zircons, although with a large dispersion, related to the evolution of the rock. This age is considered to mark the onset of granulite facies metamorphism in the Sobrado unit under intermediate-P conditions, and related to intrusive magmatism and coeval burial in a magmatic arc setting. A maximum depositional age for the Sobrado unit is established in the late Cambrian (∼ 511 Ma). The zircon dataset also record several inherited populations. The youngest cogenetic set of zircons yields crystallization ages of 546 and 526 Ma which are thought to be related to the peri-Gondwanan magmatic arc. The additional presence of inherited zircons older than 1000 Ma is interpreted as suggesting a West African Craton provenance.

1 Introduction

Zircon, monazite and titanite are accessory mineral phases found in rocks with a very wide range of compositions. These minerals can resist numerous sedimentary, igneous and metamorphic events across a wide range of temperatures, pressures and strains, even when fluids are present. Frequently, compositional domains can be defined in these minerals that record changes in different parameters (Storey et al., 2007; Castiñeiras et al., 2010; Stübner et al., 2014;

Published by Copernicus Publications on behalf of the European Geosciences Union.

Hacker et al., 2015; Stearns et al., 2016; Stipska et al., 2016). These minerals additionally provide several closed decay chains or disintegration systems ($^{238}U \rightarrow {}^{206}Pb$, $^{235}U \rightarrow {}^{207}Pb$ y $^{232}Th \rightarrow {}^{208}Pb$), because they hold variable concentrations of uranium (U) and/or thorium (Th) in their crystal lattices. Such variations in concentration allow accurate dating using microscopic-scale analysis (tens of micrometers).

Titanite is stable in metabasites across a wide range of metamorphic conditions (Spear, 1981; Frost et al., 2000) and is able to record metamorphic and deformational events (Franz and Spear, 1985; Verts and Frost, 1996; Rubatto and Hermann, 2001; Spencer et al., 2013; Stearns et al., 2015, 2016). The titanite U/Pb system is a widely used geochronometer for deformation events in granulite–amphibolite facies rocks (Spear, 1981; Cherniak, 2006; Harlov et al., 2006). Monazite is common in amphibolite and higher-grade facies. Zoning in this mineral can have an igneous or metamorphic origin (DeWolf et al., 1993; Hawkins and Bowring, 1997; Zhu et al., 1997; Spear and Pyle, 2002). The crystallization stages seen in zoned monazite, with changes in Y, Ca, Si, Sr, Ba, rare-earth elements (REEs), U and Th, has been linked to certain metamorphic reactions (Kohn and Malloy, 2004; Corrie and Kohn, 2008) or deformation process (Terry and Hamilton, 2000). Zircon survives the majority of magmatic, metamorphic and erosive terrestrial processes. Cathodoluminescence analysis of zircon zoning patterns allows a large variety of reactions to be distinguished and can clarify the petrogenetic evolution (Corfu et al., 2003). Th/U ratios can also be used to separate zircon based on their igneous or metamorphic origin (Hoskin and Ireland, 2000; Möller et al., 2002; Hokada and Harley, 2004; Hoskin, 2005). REE abundances can also be used as a qualitative petrological indicator (Belousova et al., 2002). Heavy rare-earth elements (HREEs) are preferentially incorporated into zircon compared to light rare-earth elements (LREEs). Hence, the normalized HREE slope can be used to interpret whether a zircon crystallized or recrystallized when garnet and xenotime (YPO_4) were present, because these minerals also preferentially assimilate HREE in the lattice (Hoskin and Ireland, 2000; Rubatto, 2002; Hermann and Rubatto, 2003; Rubatto et al., 2009).

The events recorded in individual grains can be radiometrically dated employing combined laser ablation analyses and cathodoluminescence (CL) images in zircons (Corfu et al., 2003) and compositional maps obtained using electron microprobe (EMPA) in monazite (Gonçalves et al., 2005; Williams et al., 2007) to recognize different growth zones. The chemical analysis, especially REE, links the development of growth zones to specific metamorphic or deformative events (Frost et al., 2000; Rubatto, 2002; Whitehouse and Platt, 2003; Zheng et al., 2007; Chen et al., 2010; Gagnevin and Daly, 2010; Holder et al., 2015;). Simultaneous geochronology and REE data are a powerful tool in the interpretation of ages – this is known as REE-assisted geochronology (Castiñeiras et al., 2010).

This methodology has been applied to selected samples of the Sobrado unit (Fig. 1), which forms part of the allochthonous complexes of NW Spain and one where the structural and metamorphic evolution is rather well known (de Pablo Maciá et al., 1984; Díaz García et al., 1999; Arenas and Martínez Catalán, 2002; Benítez-Pérez, 2017). This unit occurs in the upper allochthon of the Órdenes Complex and represents a tectonic slice of exhumed ultramafics, eclogites, high-P granulites, amphibolites and migmatitic paragneiss derived from a peri-Gondwanan terrane. It evolved along a complex sequence of geological processes involving Cambrian–Ordovician rifting with voluminous bimodal plutonism, nearly contemporaneous granulite facies metamorphism of intermediate-P, early Variscan subduction and subsequent exhumation by ductile thrusting during Variscan collision with the external margin of northern Gondwana.

Previous geochronological data on the Sobrado unit include U–Pb ages from four samples (Fernández-Suárez et al., 2002, 2007). A middle Cambrian protolith age of a gabbro and a Middle Devonian metamorphic age of a high-P basic granulite supposedly derived from the same gabbro were obtained by zircon dating. Zircon in a migmatitic, mylonitized paragneiss yielded discordant ages with an Early Ordovician lower intercept, while monazite dating provided Cambrian–Ordovician ages in another migmatitic, mylonitized paragneiss. This new study aims at constraining the metamorphic evolution of the unit including dating a migmatitic paragneiss, as previous data missed the early Variscan ages found in intercalated high-P granulites, and also an amphibolite, which could date advanced stages of exhumation. Monazite and zircon ages of paragneiss and titanite ages of amphibolites taken from separate but presently adjacent tectonic slices of the high-P/high-T (HP-HT) of the Sobrado unit are compared and interpreted using REE-assisted geochronology. This sheds new light upon the possible origin, ages and relationships between the regional foliation development and the partial melting processes that have occurred in this and equivalent units of the NW Iberian upper allochthon.

2 Geological background

The allochthonous complexes in NW Spain are remnants of a huge nappe stack preserved as klippen in the core of late Variscan synforms. They consist of units mostly of peri-Gondwanan derivation, which can be classified in three groups based on their structural position in the tectonic pile and origin: the upper, middle and lower allochthons (Fig. 1).

The upper allochthon is a piece of the northern margin of Gondwana detached and drifted away during the Cambrian–Ordovician opening of the Rheic Ocean. The middle allochthon is formed by lithospheric pieces of oceanic affinity or oceanic supracrustal sequences that formed part of the

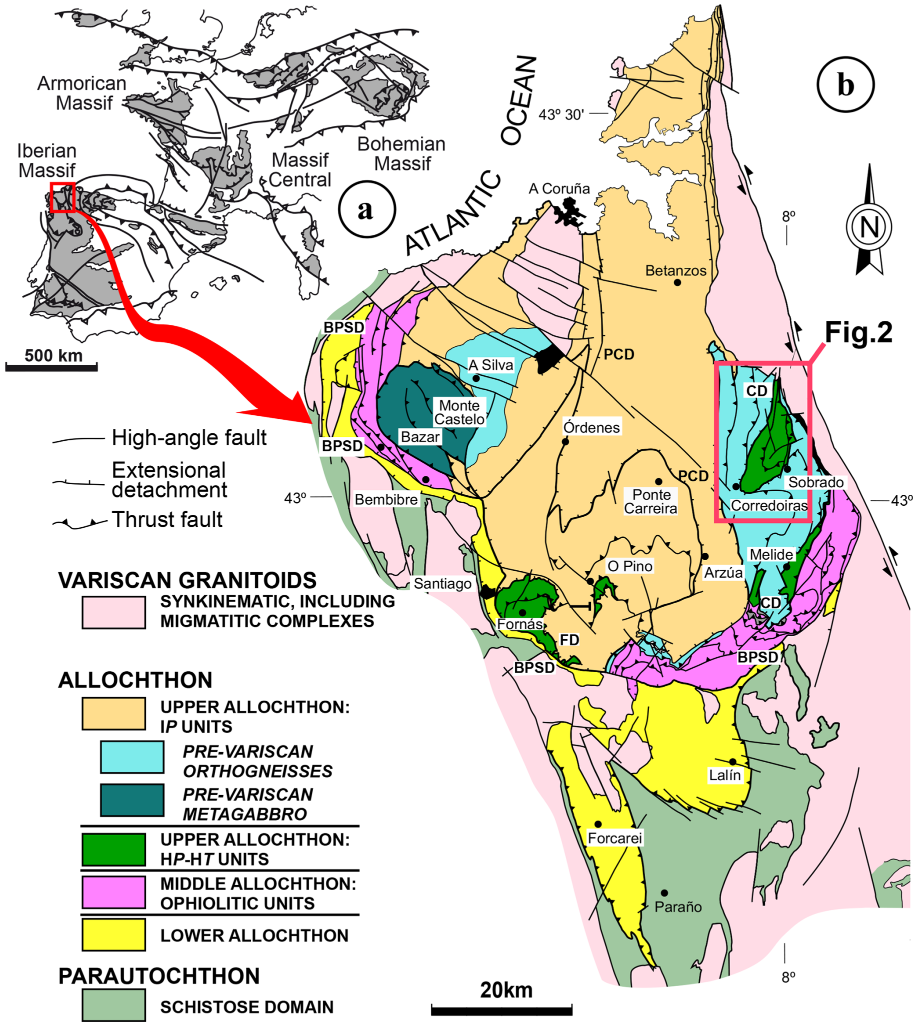

Figure 1. **(a)** Simplified map of the Variscan orogen in Europe with the location of the Órdenes Complex. **(b)** Map of the Órdenes Complex with indication of the main units and tectonic contacts. Extensional detachments are labeled: BPSD: Bembibre–Pico Sacro system; CD: Corredoiras; FD: Fornás; PCD: Ponte Carreira. Figure 2 location is indicated.

Rheic oceanic realm and are often referred to as ophiolitic units. The lower allochthon derives from distal parts of the Gondwanan continental margin.

The allochthon units are separated from the Iberian autochthon by a series of kilometer-scale imbricated sheets, known as the parautochthon (Ribeiro et al., 1990), or Schistose Domain in Galicia (NW Spain), consisting of a set of Paleozoic metasedimentary and volcanic rocks. The parautochthon has stratigraphic and igneous affinities with the Iberian autochthon of the Central Iberian Zone, and no ophiolites occur between them. For these reasons, it is interpreted as a distal part of the Gondwanan continental margin (Farias et al., 1987; Dias da Silva et al., 2014).

The allochthonous units are regarded as a stack of Variscan thrust sheets with associated tectonic fabrics and metamorphic events. Due to the “piggy-back” nature of the sequence, the structurally higher units are thought to represent the furthest traveled paleogeographic domains. Recumbent folds, thrusts and extensional detachments formed during the Variscan collision are found in all three allochthonous units (Martínez Catalán et al., 1999; Gómez-Barreiro et al., 2007).

Maximum sedimentation ages obtained from the study of detrital zircon carried out in metasediments from the upper allochthon can be estimated between 530 and 510 Ma (e.g., Fuenlabrada et al., 2010). Intrusive rocks in the upper allochthon have been dated between 520 and 490 Ma and are associated with the development of a magmatic arc which evolves into an extensional scenario that ended with the opening of the Rheic Ocean (Peucat et al., 1990; Ordóñez Casado, 1998; Abati et al., 1999, 2007; Fernández-Suárez et al., 2007; Castiñeiras et al., 2010). Two high-P/high-T metamorphic events have been recognized in this unit. The oldest one has yielded ages of 490–480 Ma (Kuijper 1979; Peucat et al. 1990; Abati et al., 1999, 2007; Fernández-Suárez et al., 2002) and the youngest one has been dated approximately between 405 and 390 Ma (Santos Zalduegui et al., 1996; Ordóñez Casado et al., 2001; Fernández-Suárez et al., 2007). In the middle allochthon, crystallization ages vary between 390 and 375 Ma (Peucat et al., 1990; Dallmeyer et al., 1991, 1997), and ages from 375 to 365 Ma have been related to continental subduction (Santos Zalduegui et al., 1995; Abati et al., 2010). Thrust wedge collapse, in the middle and lower allochthonous units, is thought to have happened between 390 and 365 Ma, followed by a collision in the internal zones around 365–330 Ma, causing further folding and thrusts (Dallmeyer et al., 1997; Martínez Catalán et al., 2009). Afterwards, there was another extensional collapse phase until 315 Ma, followed by a final phase of shortening and folding up until approximately 305 Ma related to the regional oroclinal bending in Spain (Aerden, 2004; Martínez Catalán, 2011, 2012; Álvarez-Valero et al., 2014).

The upper allochthon is further subdivided into high-P/high-T and intermediate-P units (Gómez Barreiro et al., 2007). The present study focuses on two of the high-P/high-T upper units (Figs. 1 and 2). The origin of the high-P event recorded in these units is controversial but might reflect the accretion of the units into the continental part of northern Gondwana, during the Early–Middle Devonian (400–390 Ma; Ballèvre et al., 2014).

The Sobrado antiform consists of three tectonic slices bounded by two extensional detachments (Figs. 1 and 2). The lower tectonic slice comprises highly serpentinized ultramafic rocks with interlayered metabasite units. The metabasites include eclogites (Omp + Grt + Qtz + Rt ± Ky and Zo, mineral abbreviations according to Whitney and Evans, 2010) and related clinopyroxene-garnet rocks without primary plagioclase (Cpx + Grt + Qtz + Rt ± Zo), as well as other types of rocks derived from the retrogression and mylonitization of the early high-P stages. The intermediate tectonic slice is made up of migmatitic felsic gneiss (mainly paragneiss), with frequent inclusions of high-P granulites (Cpx + Grt + Pl + Qtz + Rt ± Ky). Remnants of igneous protoliths are not preserved either in the lower or intermediate tectonic slices. The upper tectonic slice, however, contains migmatitic felsic gneiss and mafic layers derived from deformed and recrystallized gabbros with locally preserved relict igneous textures, reaching high-P granulite facies conditions. The progressive transformation from gabbros to high-P granulites (Na–Di + Grt + Pl + Qtz + Rt) has occurred in a series of different stages with a metamorphic peak at 13–17 kbar and 660–770 °C (Arenas and Martínez Catalán, 2002).

The metamorphic evolution of the Sobrado unit as described in the literature indicates that felsic gneiss underwent differing degrees of partial melting after the metabasites reached their peak pressure. Consequently, the felsic gneiss is thought to have developed a regional foliation under amphibolite facies conditions, as did the amphibolic gneiss, "flaser" amphibolites and fine-grained amphibolites. This metamorphic evolution is described by Arenas and Martínez Catalán (2002) as a clockwise P–T path, with a metamorphic peak of, at least, 15 kbar and > 800 °C, followed by an isothermal decompression. This trajectory is interpreted to result from gravitational collapse of an overthickened orogenic wedge (Gómez-Barreiro et al., 2007; Ballèvre et al., 2014). Although some regional structures, such as the Fornás detachment (FD, Fig. 1; Gómez-Barreiro et al., 2007; Álvarez-Valero et al., 2014) or the Corredoiras detachment (CD, Fig. 1; Díaz García et al., 1999), have been related to this gravitational readjustment, no study has dealt with the development of the extensional fabrics in any detail. Overall, it is thought that the extensional flow has generated a pervasive thinning of the orogenic pile and that the preserved sequence of tectonic slices is strongly condensed.

3 Sample description and methodology

3.1 Selected samples

Two representative samples (JBP-71-15A and JBP-71-21) were selected from two structurally separate but currently adjacent parts of the high-P/high-T Sobrado unit, within the Órdenes Complex, for laser ablation (laser ablation split stream; LASS) analyses, including U–Pb geochronology and REE determinations. The samples locations are presented in Fig. 2.

Sample JBP-71-21 is a mylonitic fine-grained amphibolite, without any preserved igneous relicts. Fine-grained amphibolites represent an advanced stage in the mylonitization of the metabasites. They appear as relatively thin layers inside the mafic rocks and dominate in a thick mylonitic layer (300–700 m; Fig. 2; Arenas and Martínez Catalán, 2002; Benítez Pérez, 2017) located at the base of the upper tectonic slice. The sample comprises Hbl + Pl + Grt ± Cpx + Bt ± Rt ± Ttn ± Ilm ± Zo ± Qtz (Fig. 3). Mylonitic foliation and lineation are defined by amphibole and plagioclase (Fig. 3). Garnet appears as subrounded porphyroclasts partially resorbed (Fig. 3). Titanite grains are parallel to the foliation and in textural equilibrium with plagioclase and amphibole. Rutile and ilmenite are always hosted as inclusions both in titanite and/or garnet (Fig. 3c, d).

Sample JBP-71-15A is a granulite facies migmatitic paragneiss from the underlying intermediate tectonic slice. It comprises Qtz + Pl + Grt + Kfs + Ky + Bt + Ilm + Rt and shows microscopic-scale textural evidence of partial melting. Temperature and pressure estimation ranges are 750–850 °C and 11–16 kbar for the anatectic fabric (Benítez-Pérez, 2017). Leucocratic domains with Qtz, Kfs and Pl, with evidence of plastic deformation define the foliation and Bt, Ky, Rt and Grt define linear aggregates resulting in a pervasive lineation (Fig. 4). Along the strained leucosomes, garnets show evidence of plastic deformation (Benítez Pérez, 2017) like (Fig. 4a, f, g): sigmoidal, dumbbell-shaped grains

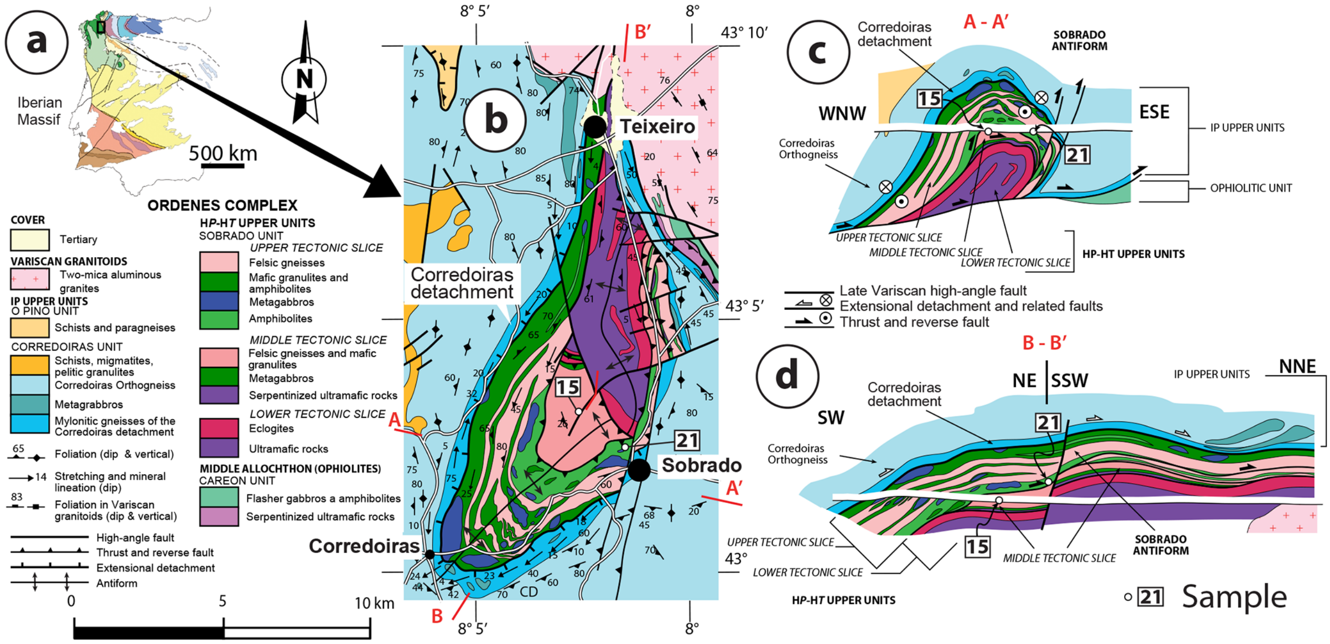

Figure 2. Geological map of the study area and location of the samples, modified from Arenas and Martínez Catalán (2002): **(a)** location of the Órdenes Complex within the Iberian massif. **(b)** Sobrado unit map, indicating units and tectonic slices. **(c)** Cross-section in the WNW–ESE direction and **(d)** SW–NE and SSW–NNE directions of the Sobrado antiform. Sample locations are indicated.

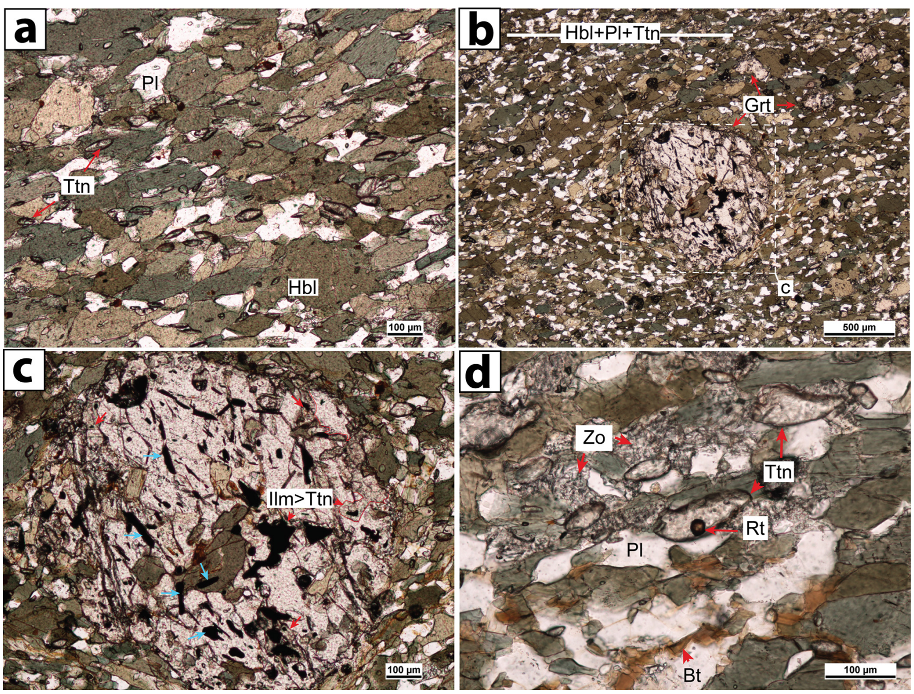

Figure 3. Fine-grained amphibolites (sample JBP-71-21) from the basal mylonitic band in the Sobrado upper tectonic slice. **(a)** Hornblende–plagioclase mixtures and titanite with preferred orientation, defining the mylonitic fabric. **(b)** Main fabric surrounding a garnet porphyroclast. Note that titanite is the Ti phase in the mylonitic fabric but ilmenite grains have been preserved inside the garnet. The position of panel **(c)** is indicated by a dashed white square. **(c)** Garnet inclusions from panel **(b)** where ilmenite inclusions show a progressive breakdown into titanite (Ilm < Ttn). Note ilmenite inclusions inside pristine garnet areas show no evidence of transformation. **(d)** Inclusions of rutile inside titanite and partial transformation of plagioclase into zoisite. All micrographs are in plane-polarized light (PPL). (Mineral abbreviations are after Whitney and Evans, 2010; Hbl: hornblende, Ttn: titanite, Ilm: ilmenite, Rt: rutile, Pl: plagioclase, Zo: zoisite, Grt: garnet.)

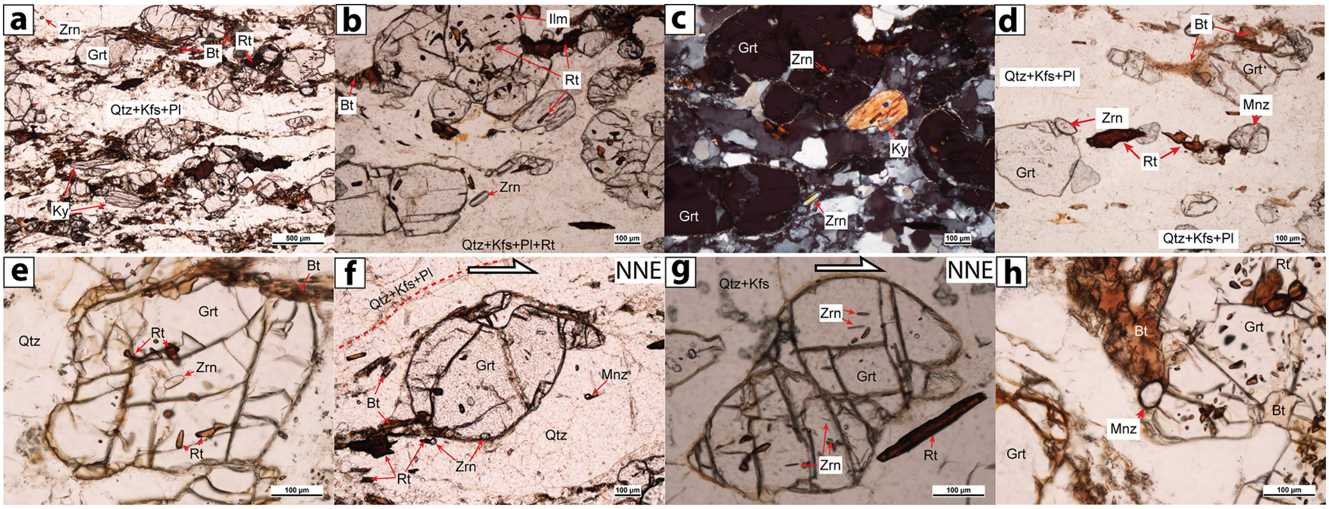

Figure 4. Granulite facies migmatitic paragneiss from the Sobrado middle tectonic slice (Fig. 2). **(a)** General microstructure where leucosome bands and preferred orientation of elongated garnets, biotite, rutile and kyanite define the foliation. **(b)** Zircon elongated grain in recrystallized leucosome domain. Main inclusions in garnet include rutile, ilmenite and zircon (PPL) and **(c)** cross-polarized light (CPL). **(d)** Monazite and zircon subrounded grain in the leucosome domain. **(e)** Subrounded elongated grain of zircon included in a garnet. **(f)** Plastically deformed garnet (sigmoidal grain) in a leucosome. Zircon and monazite are found in the quartz-rich area around the garnet. **(g)** Sigmoidal garnet in a leucosome. Inclusions of prismatic and bipyramidal zircons and rutile are observed. **(h)** Monazite grain in a garnet pressure shadow with biotite. Ky: kyanite, Bt: biotite, Qtz: quartz, Kfs: K-feldspar, Pl: plagioclase, Rt: rutile, Zrn: zircon, Mnz: monazite, Grt: garnet.

and pinch-and-swell microstructures (Ji and Martignole, 1994; Kleinschrot and Duyster, 2002; Passchier and Trouw, 2005). Zircon and monazite are found in different microtextural settings. Small elongated prims of zircon are always found shielded within garnets (Fig. 4g), while relatively larger zircon grains with irregular, elongated, subrounded shapes, appear across the fabric in leucosomes, biotite aggregates and even within kyanite crystals (Fig. 4a, b, c, d, f). In a few cases, elongated/subrounded zircons have been found as inclusions in garnets (Fig. 4e). Monazite grains show elongated to subrounded grains located in Qtz–Kfs–Pl–Bt domains, which define the main foliation of the rock (Fig. 4d, f, h).

3.2 Sample preparation

Sample preparation was carried out at the laboratories of the Universidad Complutense (Madrid). The rocks were crushed, pulverized and sieved to achieve a 0.1–0.5 mm grain size. Heavy minerals were concentrated using a Wilfley™ table. The non-magnetic minerals from this heavy fraction are then separated using a Frantz isodynamic magnetic separator. A final concentrated fraction is obtained using heavy liquids (methylene iodide, CH_2I_2).

Zircon (translucent, colorless or light brown), monazite (yellow) and titanite (colorless) grains are selected by hand-picking, according to their external morphology viewed under a binocular microscope. All the grains collected were arranged separately in parallel rows, mounted on glass slide with a double-sided adhesive and set in epoxy resin. After the resin was cured, the surface was eroded using a wet abrasive silicon carbide abrasive paper (4000 grit) and polished with 0.3 µm aluminum oxide. The surface was then coated with gold, to avoid charging problems under the scanning electron microscope (SEM). Prior to isotopic analysis, CL images of zircon grains were taken on a JEOL JSM-820 SEM, and compositional maps of monazite grains were created on a JEOL Superprobe JXA-8900M microprobe (National Center for Electron Microscopy, Madrid). Secondary electron (SE) images were also taken to determine the exact location of the spots and identify the internal structure and presence of inclusions and defects in zircon, monazite and titanite grains.

3.3 Mineral description

Titanite grains are generally rounded, with an average grain size of 100 µm and irregular morphologies. Their secondary electron images reveal homogeneous compositions and the presence of solid inclusions. This grain size permits large spatial resolution analyses (50 µm) to be carried out. Monazite grains have a more variable grain size distribution, with an average of 60–70 µm. Their habit is irregular and they usually show rounded morphologies or broken grains. We carried out La, Th, Y, U and Nd compositional maps for every monazite grain in order to discover a compositional zonation that could be attributed to different growth events. Thorium zoning is the one that developed better and was taken into account to select the spots for isotopic analysis (Fig. 5), yet it never exceeds 30 % of the grain. Several spots were analyzed in monazite crystals with the greatest compositional contrasts

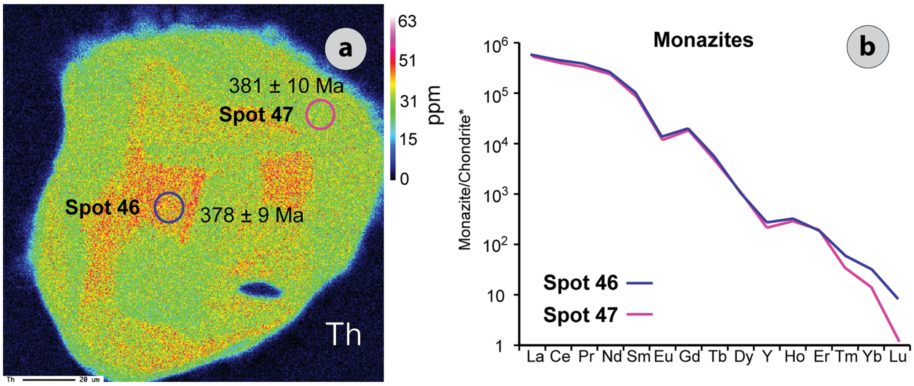

Figure 5. **(a)** Monazite grain compositional maps in paragneiss with a 30 % thorium variation. Location and spot numbers (46 and 47) are indicated, as well as the ^{206}Pb/^{238}U age and error ($\pm 2\sigma$). **(b)** Chondrite-normalized REE patterns for the same monazite in panel **(a)**.

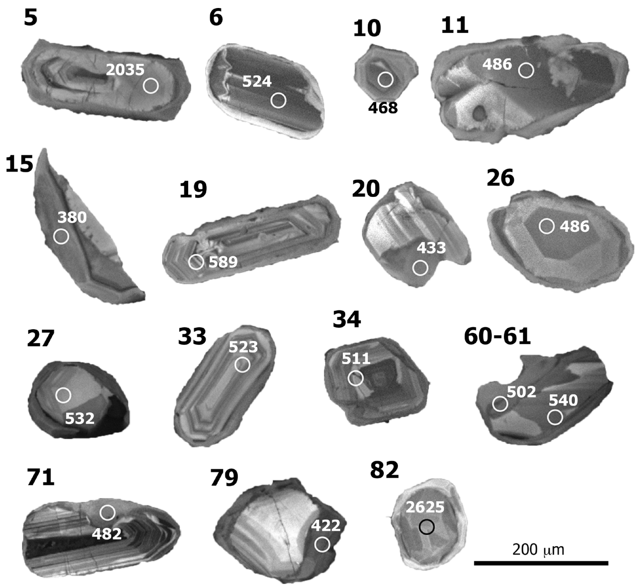

Figure 6. CL images with the location of the analyzed spots for selected zircon grains.

to determine if they really represented different growth stages in the monazite grains.

Zircon grains from the paragneiss usually have scarce mineral inclusions and they can display a wide variety of morphologies, including irregular and subrounded shapes typical of metamorphic zircon, pristine elongated dipyramidal prisms interpreted as igneous in origin and equigranular grains with abrasion signs with a probable detrital origin. Their length-to-width ratios vary between 3 : 1 and 2 : 1. Cathodoluminescence images (Fig. 6) are useful to relate the crystallization of parts of zircon crystals to specific igneous, metamorphic or deformational events (Corfu et al., 2003; Nasdala et al., 2003; Zeck et al., 2004). It is common to image a homogeneous xenocrystic core in zircon grains and even a less luminescent mantle in some grains (grain numbers 5, 6). The core aspect is mainly rounded, with irregular or angular shapes. In most of the zircon grains, the internal parts of the grains display an oscillatory zoning (grain numbers 33, 71), with different thickness, although in some cases, this zoning is faint (grain number 26). There are several grains with sector zones (grain numbers 26, 27) parallel to the zircon *c* axis (Watson and Yan Liang, 1995) and even one case of soccer-ball zoning (grain number 82). The zoning usually appears to be partially truncated and surrounded by a discontinuous poorly luminescent rim (grain numbers 20, 79).

3.4 Analytical techniques

U/Th–Pb, REE and Hf analyses of zircon, titanite and monazite were carried out using the laser ablation split stream (LASS) at the University of California at Santa Barbara (UCSB). The samples were ablated using a Photon Machines 193 nm ArF excimer ultraviolet laser with a HelEx ablation cell coupled to a Nu Instruments Plasma high-resolution multi-collector inductively coupled plasma mass spectrometer (MC-ICP-MS) and either a Nu Instruments AttoM high-resolution single-collector ICP or an Agilent 7700S quadrupole ICP-MS (Kylander-Clark et al., 2013). This installation allows the simultaneous isotopic and compositional (REE) analysis to be carried out. The laser spot diameter was 20 µm for zircon, 7–10 µm for monazite (Košler et al., 2001) and 50 µm for titanite (Stearns et al., 2016), resulting in pit depths between 6 µm for monazite and 30 µm for titanite. The laser has a fluence of $\sim 1\,\mathrm{J\,cm^{-2}}$ and was fired twice to remove common Pb from the sample surface. This material was allowed to wash out for 15 s, prior to the material being ablated at 3 Hz for 20 s for analysis. On the ICP-MS, the masses ^{204}Pb + Hg, ^{206}Pb, ^{207}Pb and ^{208}Pb were measured using ion counters, and the masses ^{232}Th and ^{238}U were measured using Faraday detectors.

The U/Th–Pb standardization for monazite was carried out using sample 44069 (Aleinikoff et al., 2006) as the primary reference material (RM), whereas the Bananeira sample was employed as primary RM for trace element corrections (Kylander-Clark et al., 2013; Palin et al., 2013). Additionally, FC-1 (Horstwood et al., 2003), Trebilcock (Tomascak et al., 1996) and Bananeira were also used as secondary monazite RM, allowing $^{206}Pb/^{238}U$ ages to be within 2 % of their accepted values. U–Pb proportions in titanite were corrected using Bear Laken (Aleinikoff et al., 2007) and Y1710C5 (Spencer et al., 2013) as RM. Overall, the 91500 sample (Wieldenbeck et al., 1995) and GJI (Jackson et al., 2004) were used as RM for zircon, both for isotopic composition and trace element calibrations. Radiogenic lead versus common lead ($^{207}Pb/^{206}Pb$) measurements require up to 2 % additional external error attributable either to variation count statistics, or ablation signal stability (Spencer et al., 2013; Hacker et al., 2015b). These external errors were incorporated into the data in the experiments.

The Iolite plug-in version 2.5 (Paton et al., 2011) from the Wavemetrics Igor Pro software was used to improve and reduce the analyses (Hacker et al., 2015). The isotopic ratios $^{238}U/^{206}Pb$ and $^{207}Pb/^{206}Pb$ for each analysis were plotted on Tera–Wasserburg diagrams (Tera and Wasserburg, 1972) using Isoplot and Topsoil programs (Ludwig, 2012; Zeringue et al., 2014). All date uncertainties are reported at the 95 % confidence interval, assuming a Gaussian distribution of measurement errors. Zircon, titanite and monazite REE analyses were normalized against the McDonough and Sun (1995) chondrite values.

4 Results

4.1 Titanite (amphibolite, upper tectonic slice)

Overall, 51 titanite analyses were projected onto a Tera–Wasserburg concordia plot (Fig. 7a). After a preliminary evaluation, 12 analyses were rejected due to either high common Pb or high discordance ($>$ 10 %) and were considered no further (Table 1). The remaining analyses define a Pb/U semi-total isochron between the common or initial Pb (^{207}Pb) and radiogenic Pb (^{206}Pb) (Ludwig, 1998). The good fit of the isochron confirms the chemical homogeneity of the data (Stearns et al., 2016) and it intercepts the concordia at 364.8 ± 4.5 Ma (2σ). Titanite chondrite-normalized REE analyses are detailed in Table 1 and are shown in Fig. 7b. Titanite REE patterns are convex upwards, relatively flat, with slight LREE depletions versus HREE with respect to chondrite. They generally lack a europium anomaly (Eu*), but some analyses show a non-distinctive positive or negative anomaly.

4.2 Monazite (paragneiss, middle tectonic slice)

For monazite U/Th−−Pb geochronology, we used the thorium zoning in monazite grains to select the analytic spots. As shown in Fig. 5, there are no significant age differences between spots or zones with different Th chemical concentrations in a single grain. The obtained REE patterns are also very similar, and the mismatch at the HREE is probably due to either uncertainties in measurement because of the lower counts or interference effects of intermediate rare-earth oxides (Holder et al., 2015).

Data from 76 U/Th−−Pb monazite analyses are shown in Table 2 and displayed using a Tera–Wasserburg concordia plot (Fig. 8a). Four of these analyses, not related to chemical zoning, were discarded due to common Pb loss and were considered no further. The remaining analyses form a single population (mean square of weighted deviation; MSWD = 0.48) centered on a concordia age of 382.5 ± 1.0 Ma (2σ). Monazite geochemistry is shown in Fig. 8b. REE patterns analyzed show an LREE enrichment, HREE depletion and negative Y anomalies with respect to chondrite with little variation within or between samples.

4.3 U–Pb zircon (paragneiss, middle tectonic slice)

Overall, 83 analyses were performed on 80 zircon grains from the Sobrado paragneiss (Table 3). In a preliminary assessment of the data, two analyses were rejected due to analytical errors (grain numbers 8 and 36). Additionally, 23 analyses yielded a discordance higher than 10 % and will not be further considered. The remaining 58 zircon analyses are shown on a Wetherill concordia plot (Fig. 9a). The $^{207}Pb/^{206}Pb$ ages older than 1000 Ma are presented in a probability density plot (Fig. 9b). Most of the old ages are distributed between 1880 and 2200 Ma, with two peaks at 2030 and 2100 Ma. Three ages are older, around 2600 Ma, and there are also two analyses around 1300 Ma. The $^{206}Pb/^{238}U$ ages younger than 1000 Ma are plotted on a Tera–Wasserburg concordia plot (Fig. 10a) and a probability density plot (Fig. 10b). The data are continuously distributed between 589 and 380 Ma and attending to their CL texture, ages from 589 to 510 Ma are obtained mainly from internal areas with oscillatory or sector zoning (e.g., 33, 27 and 62; see Fig. 6), whereas ages from 510 to 380 Ma correspond to discordant rims that have homogeneous CL signal, except for some grains (e.g., 10, 11 and 26; see Fig. 6) that are cores with oscillatory or sector zoning.

4.4 REE zircon (paragneiss, middle tectonic slice)

The chondrite-normalized REE patterns of the zircons with ages older than 600 Ma are shown in Fig. 11. In general, this group has REE patterns with a pronounced fractionation from light to heavy REE and two anomalies in Ce (positive) and in Eu (negative). There are only three analyses that diverge from this trend and show a flat HREE pattern.

For the younger analyses, the chondrite-normalized REE patterns have different features depending on the age (Fig. 12). The oldest ages (589–510 Ma) show a tight HREE fractionation, variable Eu anomaly, and a pronounced Ce

Table 1. U–Th_Pb and REE titanite_McD_ S.

Spot	238U/206Pb	^{207}Pb/^{206}Pb	208Pb/232Th	U (ppm)	Th(ppm)	La (ppm)	Ce (ppm)	Pr (ppm)	Nd (ppm)	Sm (ppm)	Eu (ppm)	Gd (ppm)	Tb (ppm)	Dy (ppm)	Ho (ppm)	Er (ppm)	Tm (ppm)	Yb (ppm)	Lu (ppm)
1	15.59 ± 0.35	0.1279 ± 0.0032	0.02292 ± 0.00053	7.42	16.57	751	1052	1182	1096	1012	1012	818	681	635	590	521	423.1	405	363.4
2	13.37 ± 0.66	0.1625 ± 0.004	0.0258 ± 0.00074	8.22	16.73	701	946	1107	1085	1128	904	889	762	661	584	483	333.6	324	232.9
3	13.74 ± 0.36	0.2123 ± 0.0056	0.03513 ± 0.00101	4.16	7.44	327	424	520	538	650	588	574	559	522	538	532	411.7	465	392.7
4	13.85 ± 0.36	0.1694 ± 0.0045	0.0514 ± 0.00298	4.3	2.47	116	188	275	318	484	519	503	471	419	408	365	278.9	299	230.5
5	13.7 ± 0.41	0.2426 ± 0.0067	0.0545 ± 0.00376	2.71	2.35	109	209	297	383	511	561	458	437	422	416	386	287.9	315	261.4
6	14.2 ± 0.4	0.1864 ± 0.0058	0.0318 ± 0.00119	3.16	4.74	225	300	369	409	547	671	515	539	495	526	511	393.5	448	383.7
7	12.06 ± 0.52	0.2955 ± 0.0111	0.15 ± 0.18002	2	1.46	68	111	153	199	314	382	329	361	373	394	399	318.6	340	290.7
8	14.52 ± 0.33	0.1863 ± 0.005	0.03051 ± 0.00091	4.86	7.93	394	574	681	705	762	813	685	648	589	608	579	436.8	504	417.1
9	15.11 ± 0.35	0.131 ± 0.0037	0.02719 ± 0.00074	6.55	10.39	471	692	733	803	861	828	714	679	636	703	693	565.6	650	561
10	12.55 ± 0.37	0.2611 ± 0.0083	0.144 ± 0.0401	2.35	0.96	45	90	152	217	359	442	328	329	300	291	304	252.6	290	245.5
11	15.48 ± 0.35	0.1264 ± 0.0034	0.0334 ± 0.00137	8.13	6.22	350	654	938	1120	1201	1107	1045	928	902	890	901	659.9	711	586.6
12	7.3 ± 1.08	0.471 ± 0.0153	0.072 ± 0.09601	0.61	0.32	15	27	42	67	134	140	162	189	215	233	264	248.2	287	232.1
13	10.02 ± 0.47	0.4211 ± 0.0111	0.112 ± 0.09503	1.2	0.69	31	61	98	139	244	209	230	214	156	108	93	78.5	80	72.8
14	9.66 ± 0.47	0.387 ± 0.0135	0.22 ± 0.17006	1.09	0.56	29	55	79	96	159	197	160	181	200	213	249	230.4	296	242.7
15	13.99 ± 0.32	0.191 ± 0.0046	0.03377 ± 0.00107	4.58	6.1	184	317	421	512	599	485	518	467	433	401	374	319.8	306	236.2
16	14.41 ± 0.41	0.1672 ± 0.0063	0.0315 ± 0.00144	4.02	5.44	216	359	421	492	642	501	609	609	590	549	545	471.3	464	395.9
17	14.94 ± 0.36	0.1761 ± 0.0048	0.13 ± 0.03609	4.38	0.71	43	108	170	239	404	460	433	485	572	540	536	488.3	420	339
18	7.35 ± 0.77	0.549 ± 0.0155	−0.08 ± −0.14001	0.55	0.3	18	26	36	42	68	68	77	92	122	141	181	210.9	230	204.5
19	15.96 ± 0.36	0.1397 ± 0.0034	0.0271 ± 0.00071	8.1	9.22	414	520	541	580	692	609	652	624	708	579	591	630.8	507	405.7
20	15.04 ± 0.36	0.1649 ± 0.0049	0.03031 ± 0.00096	6.39	8.79	293	426	468	522	543	499	482	455	514	419	438	446.6	412	321.1
21	11.9 ± 0.34	0.3127 ± 0.0079	0.37 ± 0.22012	2.91	0.4	48	108	185	276	507	426	527	465	385	218	153	120.2	80	59.3
22	14.41 ± 0.34	0.194 ± 0.0054	0.0514 ± 0.00216	5.29	3.73	255	465	598	716	889	794	766	709	817	603	595	629.1	472	382.1
23	14.18 ± 0.37	0.1682 ± 0.0046	0.098 ± 0.01612	4.77	1.43	102	228	355	458	710	718	687	604	671	488	476	449.4	344	258.5
24	15.92 ± 0.35	0.1147 ± 0.003	0.02388 ± 0.00057	10.78	13.2	468	695	829	915	901	1052	731	604	620	458	442	428.3	323	278
25	7.63 ± 0.83	0.512 ± 0.015	−0.03 ± −0.49	0.68	0.14	9	21	37	56	110	157	147	157	209	182	211	270.4	234	214.2
26	12.27 ± 0.5	0.32 ± 0.0119	0.0577 ± 0.00542	1.68	2.17	93	148	203	243	286	325	275	274	313	271	307	349	312	285.4
27	14.67 ± 0.35	0.1937 ± 0.0048	0.03279 ± 0.00098	4.67	6.77	354	560	653	700	703	639	652	551	557	401	347	332.8	248	162.6
28	15.2 ± 0.46	0.1543 ± 0.0069	0.0335 ± 0.00183	4.88	4.43	174	326	463	554	642	542	593	512	581	487	521	521.1	496	453.7
29	14.56 ± 0.31	0.112 ± 0.0029	0.02158 ± 0.00049	11.71	22.45	495	625	696	722	728	886	653	584	642	562	575	536	444	363
30	10.92 ± 0.38	0.3387 ± 0.0094	0.0584 ± 0.00378	1.54	2.51	111	129	147	168	229	267	270	312	375	364	431	455.9	451	411
31	10.64 ± 0.67	0.368 ± 0.0132	0.122 ± 0.03409	1.07	0.81	29	58	84	114	158	173	195	184	230	228	262	283	270	259.3
32	9.39 ± 0.5	0.443 ± 0.0141	−0.02 ± −0.12	0.9	0.58	22	42	61	81	130	179	152	162	207	205	242	246.2	289	248.8
33	10.49 ± 0.65	0.3651 ± 0.0111	0.095 ± 0.00969	1.13	1.22	55	82	100	120	149	189	163	162	203	196	229	210.5	247	236.6
34	15.19 ± 0.35	0.1501 ± 0.004	0.042 ± 0.00163	5.56	3.48	235	434	593	696	705	801	639	537	517	454	488	390.3	419	399.2
35	14.53 ± 0.41	0.1866 ± 0.0067	0.0339 ± 0.00129	3.69	4.89	172	263	322	383	457	471	483	465	516	482	494	401.6	464	401.2
36	14.66 ± 0.36	0.1785 ± 0.0047	0.0584 ± 0.00378	4.36	2.21	111	252	399	514	703	588	649	544	524	463	461	351.8	391	368.3
37	16.03 ± 0.34	0.1359 ± 0.0032	0.0472 ± 0.0023	8.41	3.38	281	400	473	503	493	611	443	355	366	321	320	264.8	297	287.8
38	10.52 ± 0.48	0.3435 ± 0.0113	0.144 ± 0.06906	1.28	0.55	22	40	63	93	172	221	236	293	370	352	385	304	348	308.1
39	8.65 ± 0.61	0.496 ± 0.0164	0 ± 0	0.66	0.24	9	17	29	37	83	123	126	158	215	232	284	215.8	278	267.9
40	15.85 ± 0.34	0.116 ± 0.0028	0.02681 ± 0.0008	7.59	7.2	348	566	735	869	950	1151	862	731	739	619	632	420.2	530	460.6
41	11.89 ± 0.31	0.1654 ± 0.0046	0.06 ± 0.14001	2.54	0.09	16	60	148	259	580	512	585	518	511	425	428	291.9	411	362.2
42	9.82 ± 0.57	0.4175 ± 0.0124	0.138 ± 0.08205	0.95	0.79	71	99	105	105	98	210	94	87	100	89	104	74.5	115	122
43	15.67 ± 0.34	0.1411 ± 0.0037	0.02576 ± 0.00068	6.21	10.38	640	799	852	832	803	913	671	607	625	520	493	319.8	397	362.2
44	11.01 ± 0.57	0.3661 ± 0.0111	0.11 ± 0.14002	1.2	0.86	34	57	75	99	154	196	174	218	270	274	316	272.5	369	345.9
45	7.67 ± 0.6	0.484 ± 0.0139	0.04 ± 0.25	0.57	0.33	20	33	42	58	105	123	136	150	193	200	221	204	263	280.5
46	13.25 ± 0.39	0.2117 ± 0.0071	0.0379 ± 0.00242	2.61	4.41	228	284	304	324	395	455	384	348	358	302	284	195.5	227	204.9
47	10.78 ± 0.54	0.2924 ± 0.0105	0.133 ± 0.07405	1.66	0.79	37	79	118	165	255	304	277	309	340	313	321	253.8	305	288.2
48	6.94 ± 0.74	0.511 ± 0.0158	0.0745 ± 0.0057	0.64	1.89	173	290	339	376	356	230	303	269	273	260	255	186.6	217	199.2
49	15.64 ± 0.33	0.1197 ± 0.0028	0.03214 ± 0.001	10.32	7.5	521	772	845	886	937	1130	839	676	683	551	478	336	339	299.2
50	10.66 ± 0.43	0.3635 ± 0.0094	0.0697 ± 0.00481	1.77	2.45	197	218	213	235	245	269	259	261	294	258	279	210.9	246	236.6
51	7.32 ± 0.55	0.569 ± 0.0158	0.0894 ± 0.0082	0.7	1.76	183	217	191	182	143	85	107	102	102	101	107	92.3	114	118.7

Table 2. U–Th_Pb and REE monazite_McD_S.

Spot	238U/206Pb	$^{207}Pb/^{206}Pb$	208Pb/232Th	U (ppm)	Th (ppm)	La (ppm)	Ce (ppm)	Pr (ppm)	Nd (ppm)	Sm (ppm)	Eu (ppm)	Gd (ppm)	Tb (ppm)	Dy (ppm)	Y (ppm)	Ho (ppm)	Er (ppm)	Tm (ppm)	Yb (ppm)	Lu (ppm)
1	16.29 ± 0.35	0.0543 ± 0.0013	0.01930 ± 0.00041	1640	26 200	554 430	433 931	365 302	243 982	98 243	12 131	19 899	4429	992	243	273	170	32.4	20	3.3
2	16.28 ± 0.35	0.0545 ± 0.0013	0.01916 ± 0.00042	1850	29 300	527 004	437 194	352 371	242 451	94 324	13 286	19 749	4490	1081	272	322	191	27.5	25	0.0
3	16.20 ± 0.38	0.0544 ± 0.0012	0.01949 ± 0.00044	2300	25 500	519 409	420 881	346 983	250 109	107 905	12 451	23 869	5319	1163	282	374	190	71.7	8	24.8
4	16.30 ± 0.38	0.0546 ± 0.0013	0.01930 ± 0.00047	1454	34 200	563 713	425 775	323 276	223 632	85 270	11 474	18 543	4266	898	192	251	118	46.6	6	12.2
5	16.18 ± 0.36	0.0543 ± 0.0012	0.01926 ± 0.00043	1805	32 400	547 257	420 881	353 448	231 947	92 568	11 385	19 899	4197	959	179	260	143	38.1	14	0.0
6	16.09 ± 0.35	0.0541 ± 0.0013	0.01946 ± 0.00044	1660	25 900	524 051	409 462	338 362	238 074	96 622	11 794	19 045	4634	980	227	291	184	44.5	19	5.7
7	16.27 ± 0.36	0.0544 ± 0.0012	0.01938 ± 0.00045	1790	29 000	554 430	442 088	369 612	230 853	95 676	12 647	19 598	4072	1045	248	310	172	46.6	20	30.5
8	16.15 ± 0.36	0.0545 ± 0.0012	0.01920 ± 0.00042	2170	44 100	579 325	437 194	359 914	248 796	97 838	13 179	18 693	3875	927	203	306	182	42.1	12	8.1
9	16.22 ± 0.37	0.0558 ± 0.0012	0.01900 ± 0.00043	2150	47 100	567 511	422 512	340 517	245 295	90 608	12 451	17 789	3958	902	232	286	179	52.2	6	25.6
10	16.38 ± 0.38	0.0549 ± 0.0012	0.01940 ± 0.00045	1680	27 900	526 160	435 563	357 759	242 451	93 919	12 664	19 799	4078	947	210	264	143	46.2	11	8.9
11	16.20 ± 0.37	0.0547 ± 0.0012	0.01930 ± 0.00044	1950	35 700	555 274	433 931	383 621	254 923	95 270	12 060	19 296	4432	996	221	321	181	44.1	17	5.7
12	16.29 ± 0.37	0.0546 ± 0.0012	0.01915 ± 0.00044	2280	32 800	555 274	415 987	336 207	252 298	103 176	13 215	20 201	4510	976	236	280	195	39.7	7	0.0
13	16.35 ± 0.38	0.0548 ± 0.0012	0.01897 ± 0.00044	2230	43 200	540 928	411 093	349 138	246 827	94 662	12 202	18 643	4551	976	218	282	138	36.0	13	0.0
14	16.28 ± 0.36	0.0545 ± 0.0012	0.01908 ± 0.00043	2060	41 000	564 135	438 825	362 069	230 197	95 608	12 575	19 296	4269	866	209	251	162	16.2	13	11.8
15	16.31 ± 0.39	0.0545 ± 0.0012	0.01920 ± 0.00045	2020	29 600	535 865	450 245	378 233	242 888	109 932	13 268	22 412	5125	1085	264	335	179	56.7	16	8.1
16	16.23 ± 0.36	0.0544 ± 0.0012	0.01953 ± 0.00044	1714	31 400	562 447	460 033	391 164	261 050	103 514	13 748	19 196	4432	988	211	244	182	37.2	14	12.2
17	16.40 ± 0.36	0.0546 ± 0.0012	0.01910 ± 0.00045	2360	37 500	565 401	429 038	366 379	241 357	96 689	12 398	18 894	4352	1004	218	291	177	25.5	10	8.9
18	16.22 ± 0.36	0.0545 ± 0.0012	0.01943 ± 0.00043	1662	30 800	580 591	464 927	376 078	262 363	100 000	12 256	18 894	4654	1081	228	308	168	48.2	17	3.3
19	16.25 ± 0.38	0.0538 ± 0.0013	0.01932 ± 0.00046	1600	31 200	618 143	442 088	383 621	244 420	101 419	12 593	20 050	4399	1024	217	253	161	34.0	4	2.8
20	16.11 ± 0.35	0.0545 ± 0.0012	0.01915 ± 0.00042	2190	34 200	567 932	427 406	364 224	240 919	101 351	12 611	19 899	4598	1012	238	300	201	30.8	18	6.9
21	16.17 ± 0.35	0.0543 ± 0.0012	0.01926 ± 0.00045	1804	28 900	537 975	443 719	365 302	243 326	100 608	13 428	18 693	4197	951	208	286	153	39.7	17	3.3
22	16.08 ± 0.35	0.0543 ± 0.0012	0.01964 ± 0.00044	2380	38 200	560 338	448 613	383 621	249 672	101 554	12 913	19 497	5125	1065	222	308	167	21.1	16	9.3
23	16.08 ± 0.37	0.0594 ± 0.0016	0.01886 ± 0.00044	1704	84 000	562 447	391 517	327 586	231 947	87 635	12 487	16 281	4019	951	246	264	215	68.0	30	40.7
24	16.18 ± 0.39	0.0536 ± 0.0012	0.01938 ± 0.00049	1650	29 500	541 772	417 618	359 914	238 731	97 230	12 647	18 693	4529	1110	246	315	188	31.2	19	11.0
25	16.37 ± 0.39	0.0546 ± 0.0012	0.01876 ± 0.00045	1900	578 00	564 557	417 618	337 284	232 604	94 797	11 634	16 935	4030	894	217	295	148	79.4	12	3.7
26	16.43 ± 0.38	0.0550 ± 0.0013	0.01922 ± 0.00044	1663	27 800	566 667	422 512	360 991	243 545	97 635	12 700	17 236	4488	963	249	288	184	56.3	8	14.6
27	16.32 ± 0.39	0.0549 ± 0.0012	0.01934 ± 0.00049	2000	32 900	575 949	432 300	354 526	249 453	100 608	13 250	19 347	4958	1167	255	306	177	47.8	17	7.3
28	16.35 ± 0.38	0.0538 ± 0.0011	0.01948 ± 0.00046	3680	28 300	582 700	445 351	363 147	264 770	118 243	15 062	25 025	6648	1553	383	443	213	45.7	25	16.7
29	16.58 ± 0.35	0.0539 ± 0.0011	0.01908 ± 0.00044	3050	32 100	551 899	432 300	385 776	240 044	118 243	14 512	24 171	6427	1451	352	399	221	43.3	16	7.7
30	16.27 ± 0.38	0.0546 ± 0.0012	0.01941 ± 0.00046	1822	27 600	562 447	440 457	375 000	260 394	104 054	13 694	21156	5235	1102	240	332	191	30.4	24	16.7
31	16.63 ± 0.40	0.0544 ± 0.0013	0.01874 ± 0.00045	1926	28 200	570 042	437 194	350 216	232 604	99 324	11 261	18 693	4432	992	211	288	196	51.8	18	3.3
32	16.68 ± 0.42	0.0546 ± 0.0012	0.01915 ± 0.00047	2130	35 500	542 194	419 250	371 767	248 359	102 703	13 144	18 191	4834	996	243	291	168	47.8	21	0.0
33	16.36 ± 0.37	0.0541 ± 0.0012	0.01936 ± 0.00044	2220	29 500	556 540	414 356	369 612	257 987	100 338	13 197	20 402	4709	1053	248	300	174	39.3	8	13.4
34	16.42 ± 0.39	0.0544 ± 0.0012	0.01944 ± 0.00047	1950	30 300	587 342	407 830	355 603	255 580	100 000	12 824	19 648	4598	1041	253	289	166	21.9	16	18.3
35	16.39 ± 0.41	0.0542 ± 0.0012	0.01944 ± 0.00050	2480	32 400	562 025	412 724	367 457	245 514	113 446	14 725	24 372	6427	1439	341	452	231	64.4	16	24.8
36	16.31 ± 0.36	0.0544 ± 0.0013	0.01912 ± 0.00041	2010	43 900	580 591	402 936	355 603	258 425	90 405	10 533	16 935	4460	850	208	242	168	49.4	3	3.3
37	16.34 ± 0.44	0.0552 ± 0.0013	0.01948 ± 0.00050	2200	42 200	582 700	435 563	365 302	247 046	100 811	13 002	21 809	5512	1150	239	295	179	33.2	35	9.3
38	16.54 ± 0.38	0.0543 ± 0.0012	0.01913 ± 0.00049	2148	44 200	571 308	414 356	363 147	241 794	92 770	11 829	18 543	4645	1008	214	286	162	49.4	24	8.9
39	16.39 ± 0.44	0.0550 ± 0.0014	0.01960 ± 0.00053	1419	32 800	565 823	443 719	365 302	249 234	91 014	11 901	16 935	4598	907	222	267	157	51.8	22	6.1
40	16.44 ± 0.39	0.0542 ± 0.0013	0.01949 ± 0.00047	1930	31 600	556 540	424 144	382 543	257 112	96 757	12 504	19 598	4903	1175	256	326	203	45.3	17	20.7
41	16.37 ± 0.38	0.0548 ± 0.0012	0.01928 ± 0.00044	1690	40 600	562 447	435 563	387 931	262 363	85 405	11 332	18 342	4571	1045	239	333	178	41.3	28	13.4
42	16.56 ± 0.41	0.0544 ± 0.0013	0.01950 ± 0.00050	1655	34 400	573 418	420 881	350 216	243 107	92 095	12 131	19 246	4654	1037	231	321	164	27.9	12	0.0
43	16.26 ± 0.37	0.0545 ± 0.0013	0.01927 ± 0.00044	2490	37 200	569 198	432 300	383 621	245 952	88 108	10 728	18291	4211	915	204	286	164	21.5	16	13.8
44	16.33 ± 0.40	0.0540 ± 0.0012	0.01942 ± 0.00047	2260	30 300	585 654	437 194	376 078	267 396	95 338	14 369	19 950	4737	1089	232	300	160	49.4	9	8.5
45	16.22 ± 0.37	0.0542 ± 0.0013	0.01942 ± 0.00045	1600	44 700	528 692	414 356	329 741	239 168	87 365	10 906	18 945	4820	1057	245	326	183	11.7	23	0.0
46	16.57 ± 0.41	0.0539 ± 0.0013	0.01907 ± 0.00049	1674	39 800	538 397	402 936	328 664	237 199	85 135	11 812	18 342	4681	1089	215	289	195	34.4	14	0.0
47	16.44 ± 0.42	0.0535 ± 0.0012	0.01927 ± 0.00048	1920	30 300	528 692	417 618	351 293	243 326	94 054	12 771	18 593	5208	1000	262	311	180	57.5	31	8.1
48	16.39 ± 0.40	0.0533 ± 0.0012	0.01936 ± 0.00049	1789	31 400	540 928	446 982	350 216	240 263	89 189	12 220	17 538	4349	898	202	317	151	21.5	19	5.7
49	16.21 ± 0.37	0.0553 ± 0.0013	0.01947 ± 0.00046	1810	35 800	570 464	430 669	375 000	262 582	99 459	12 824	21 859	5125	1264	283	308	190	24.7	8	2.4
50	16.40 ± 0.37	0.0543 ± 0.0012	0.01944 ± 0.00045	2020	31 600	561 603	411 093	340 517	233 479	92 838	12 131	19 196	4598	1000	219	337	168	21.5	14	16.7
51	16.66 ± 0.40	0.0534 ± 0.0011	0.01944 ± 0.00047	4730	33 200	523 207	432 300	303 879	243 545	110 135	14 512	25 879	6759	1650	358	575	217	79.8	31	7.7
52	16.54 ± 0.40	0.0540 ± 0.00122	0.01953 ± 0.000469	1900	36 500	585 654	474 715	359 914	258 425	111 283.8	14547	21859	5983	1341	318	410	239	69.6	35.4	13.4
53	16.61 ± 0.42	0.0544 ± 0.00132	0.01891 ± 0.000502	1596	66 200	545 992	412 398	295 259	233 260	84 932.43	11 758	18 593	4391	1085	255	308	212	30.0	11.2	5.3
54	16.49 ± 0.39	0.0569 ± 0.00129	0.01916 ± 0.000475	1611	57 800	542 616	437 194	352 371	244 201	100 202.7	13 499	20 804	4931	1081	232	350	159	36.4	21.7	8.1
55	16.34 ± 0.48	0.0537 ± 0.00125	0.01950 ± 0.000545	1760	30 200	581 013	476 346	371 767	246 827	94 729.73	13 357	19 899	4377	1024	193	251	169	32.8	25.5	5.7
56	16.80 ± 0.40	0.0541 ± 0.00115	0.01912 ± 0.000446	2240	37 600	536 709	438 825	335 129	235 449	84 797.3	11 758	16 985	4177	996	204	288	164	40.9	28.6	8.1
57	16.49 ± 0.41	0.0540 ± 0.00113	0.01979 ± 0.000522	3610	30 800	526 160	461 664	355 603	247 484	111 621.6	13 979	26 533	6648	1602	318	447	240	51.0	49.7	18.3
58	16.33 ± 0.40	0.0544 ± 0.00121	0.01965 ± 0.000471	2110	39 100	568 354	464 927	329 741	240 700	80 000	11 279	16 030	3767	748	165	216	128	38.9	16.8	0.0
59	16.59 ± 0.38	0.0542 ± 0.0012	0.01946 ± 0.000442	3130	33 400	556 118	461 664	344 828	250 985	93 648.65	11 883	19 698	4873	976	222	271	173	42.9	13.0	19.5
60	16.59 ± 0.38	0.0540 ± 0.0012	0.01944 ± 0.000447	3270	30 600	567 511	450 245	322 198	245 733	111 283.8	13 854	23 819	5956	1524	323	445	236	36.4	16.8	19.5
61	16.55 ± 0.42	0.0537 ± 0.00124	0.01905 ± 0.00045	1860	695 00	540 928	433 931	309 267	224 508	87 702.7	12 256	16 683	3518	752	174	209	156	36.4	6.8	13.4
62	16.14 ± 0.40	0.0538 ± 0.00114	0.01945 ± 0.000517	3700	34 000	579 325	481 240	346 983	233 260	114 189.2	14 760	25226	6288	1467	359	498	232	72.1	27.3	32.5
63	16.35 ± 0.38	0.0539 ± 0.00121	0.01971 ± 0.000462	2030	32 300	582 700	477 977	342 672	245 733	94 256.76	13 464	18 894	4343	967	227	255	166	38.9	36.6	8.9
64	16.45 ± 0.44	0.0554 ± 0.00135	0.01954 ± 0.000525	1700	32 600	584 388	461 664	345 905	228 665	100 000	12 398	22 010	5457	1248	287	397	194	44.9	22.4	14.2
65	16.59 ± 0.40	0.0538 ± 0.00132	0.01921 ± 0.00047	1476	33 600	602 532	453 507	372 845	246 827	88 648.65	12 007	18 794	4609	988	210	277	182	65.2	19.9	13.8
66	16.37 ± 0.41	0.0588 ± 0.00127	0.01931 ± 0.000483	1900	42 200	518 987	451 876	314 655	231 072	82 297.3	12 575	16 432	3449	833	164	212	144	8.9	17.4	0.0
67	16.36 ± 0.40	0.0541 ± 0.00114	0.01942 ± 0.000473	2520	30 760	554 008	451 876	355 603	263 020	112 702.7	15 293	23 266	5789	1362	313	401	203	46.6	21.7	19.1
68	16.58 ± 0.40	0.0536 ± 0.00114	0.01947 ± 0.000486	4360	30 500	551 055	445 351	365 302	253 611	106 891.9	12 895	21 859	5180	1167	253	342	175	54.3	10.6	2.8
69	16.48 ± 0.36	0.0544 ± 0.00126	0.01949 ± 0.000443	2458	38 700	540 506	474 715	376 078	270 460	98 175.68	12 860	19 598	4571	1020	230	319	166	40.5	14.3	13.0
70	16.53 ± 0.39	0.0532 ± 0.00121	0.01933 ± 0.00046	2109	32 100	576 371	450 408	367 457	266 521	106 081.1	13 606	20 251	4535	1053	232	317	178	28.3	21.7	0.0
71	16.45 ± 0.44	0.0542 ± 0.0013	0.01924 ± 0.00052	1890	47 000	562 447	438 825	335 129	252 079	98 310.81	12 877	19 246	4321	959	221	321	186	34.0	13.7	19.1
72	16.48 ± 0.42	0.0544 ± 0.00118	0.01953 ± 0.000499	1660	34 700	583 966	491 028	385 776	286 433	96 013.51	13 819	19 749	4488	1179	283	364	203	44.5	15.5	8.5
73	16.27 ± 0.40	0.0557 ± 0.00123	0.01927 ± 0.000501	1970	86 900	597 046	405 057	315 733	243 107	80 135.14	11 545	15 829	3399	813	159	214	136	31.6	16.1	11.8
74	16.18 ± 0.41	0.0540 ± 0.00127	0.01937 ± 0.000484	2270	37 100	594 937	442 088	334 052	248 578	89 054.05	12 078	18 492	3853	833	192	251	157	15.0	16.8	13.4
75	16.17 ± 0.38	0.0535 ± 0.00122	0.01985 ± 0.000459	2460	31 100	580 591	451 876	365 302	266 740	116 216.2	14 174	23 317	5568	1276	276	394	232	25.5	26.1	14.6
76	16.11 ± 0.38	0.0542 ± 0.00126	0.01946 ± 0.000452	1563	33 400	582 278	446 982	348 060	269 147	104 729.7	14 121	20 251	4479	984	219	271	175	22.3	9.3	8.9

Table 3. U–Th_Pb zircon sorted by age.

Spot	Location	U (ppm)	Th (ppm)	Th/U	^{207}Pb/^{235}U	2σ	^{206}Pb/^{238}U	2σ	^{207}Pb/^{206}Pb	2σ	ρ	^{207}Pb/^{235}U Age (Ma)	2σ	^{206}Pb/^{238}U Age (Ma)	2σ	^{207}Pb/^{206}Pb Age (Ma)	2σ	Probability of concordance
3	Core	690	223	0.32	10 760	0.242	0.423	0.0093	0.184	0.004	−0.05	2502	9	2272	18	2691	6	0.91
72		495	22	0.04	10.230	0.273	0.421	0.0111	0.174	0.004	0.06	2455	16	2264	33	2596	6	0.92
82		280	136	0.48	9.840	0.281	0.403	0.0112	0.177	0.004	−0.36	2418	19	2183	36	2625	5	0.90
80		46	34	0.74	6.460	0.176	0.364	0.0095	0.128	0.003	−0.06	2039	17	1998	29	2065	8	0.98
40		62	40	0.64	6.390	0.182	0.358	0.0097	0.130	0.003	−0.31	2030	18	1974	31	2095	9	0.97
37		151	53	0.35	6.426	0.151	0.358	0.0082	0.131	0.003	−0.19	2035	11	1972	19	2107	7	0.97
44		100	109	1.09	6.100	0.193	0.356	0.0108	0.124	0.003	−0.14	1989	21	1960	38	2020	8	0.99
2	Rim	444	141	0.32	8.210	0.198	0.355	0.0082	0.168	0.003	−0.31	2256	12	1958	19	2542	4	0.87
5		70	102	1.47	5.854	0.150	0.342	0.0090	0.125	0.003	0.01	1957	15	1895	28	2035	9	0.97
28		878	74	0.08	7.890	0.218	0.334	0.0090	0.173	0.004	−0.07	2218	18	1858	30	2584	10	0.84
48		28	15	0.53	6.030	0.251	0.334	0.0137	0.130	0.003	−0.12	1976	32	1856	58	2098	15	0.94
32		101	49	0.49	5.867	0.153	0.333	0.0085	0.129	0.003	0.18	1956	14	1853	26	2080	10	0.95
18		49	19	0.38	5.977	0.155	0.321	0.0083	0.137	0.003	0.03	1975	16	1799	23	2184	12	0.91
4		677	299	0.44	5.659	0.146	0.316	0.0080	0.130	0.003	−0.30	1924	14	1767	24	2103	5	0.92
83		48	22	0.47	5.510	0.163	0.314	0.0093	0.127	0.003	0.10	1906	20	1762	34	2056	15	0.93
39		125	113	0.90	5.190	0.144	0.309	0.0082	0.122	0.003	−0.39	1849	17	1737	27	1987	9	0.94
49		403	115	0.29	6.840	0.196	0.307	0.0083	0.161	0.003	−0.10	2090	18	1732	29	2466	9	0.83
35		182	124	0.68	5.660	0.158	0.298	0.0078	0.138	0.003	−0.22	1924	17	1683	25	2204	13	0.87
51		304	97	0.32	5.366	0.145	0.297	0.0079	0.131	0.003	−0.13	1878	16	1676	26	2111	5	0.89
66		693	223	0.32	6.470	0.176	0.295	0.0079	0.158	0.003	−0.11	2041	17	1664	26	2433	5	0.82
21		587	251	0.43	5.019	0.124	0.294	0.0070	0.125	0.003	−0.25	1824	12	1663	19	2028	5	0.91
16		118	107	0.91	5.043	0.126	0.294	0.0071	0.125	0.003	−0.23	1826	13	1660	20	2032	9	0.91
65		407	6	0.02	4.481	0.111	0.270	0.0067	0.120	0.002	0.15	1730	11	1539	20	1956	5	0.89
1		52	36	0.70	4.496	0.129	0.266	0.0072	0.122	0.003	−0.26	1729	17	1524	24	1995	14	0.88
22		128	32	0.25	4.144	0.103	0.266	0.0065	0.115	0.002	−0.13	1663	12	1519	19	1881	10	0.91
24		166	71	0.43	4.140	0.154	0.260	0.0086	0.117	0.002	−0.72	1660	25	1490	35	1910	12	0.90
54		66	43	0.64	4.218	0.118	0.253	0.0070	0.121	0.003	−0.09	1677	16	1452	25	1975	13	0.87
81		80	47	0.59	4.091	0.115	0.246	0.0068	0.120	0.003	0.00	1652	16	1417	24	1960	12	0.86
23		71	51	0.71	4.060	0.162	0.244	0.0080	0.121	0.003	−0.50	1650	29	1406	33	1979	15	0.85
31		41	17	0.41	3.840	0.134	0.236	0.0072	0.118	0.003	−0.29	1600	23	1367	28	1931	16	0.85
38		48	27	0.56	2.564	0.088	0.214	0.0072	0.087	0.002	0.00	1289	20	1251	31	1372	20	0.97
58		463	39	0.08	3.354	0.099	0.210	0.0060	0.116	0.002	−0.39	1496	18	1228	23	1903	10	0.82
46		275	126	0.46	2.377	0.068	0.208	0.0059	0.082	0.002	−0.19	1235	15	1219	22	1252	8	0.99
50		321	114	0.35	3.216	0.091	0.205	0.0059	0.115	0.002	−0.13	1463	16	1202	23	1876	8	0.82
9		53	45	0.84	2.485	0.076	0.170	0.0049	0.106	0.002	0.04	1267	17	1011	20	1724	17	0.80
41		36	16	0.45	2.302	0.077	0.156	0.0052	0.107	0.003	0.07	1211	19	935	23	1754	23	0.77
45		65	29	0.45	2.113	0.072	0.153	0.0047	0.100	0.002	−0.17	1152	19	919	20	1620	18	0.80
30		270	29	0.11	1.994	0.083	0.146	0.0049	0.099	0.002	−0.73	1111	25	878	22	1607	20	0.79
78		157	40	0.26	1.241	0.040	0.111	0.0031	0.081	0.002	−0.30	818	14	677	13	1215	19	0.83
77		397	18	0.05	1.284	0.042	0.111	0.0033	0.084	0.002	−0.40	838	15	675	14	1287	10	0.81
73		238	34	0.14	1.054	0.042	0.097	0.0028	0.077	0.002	−0.57	730	17	597	12	1121	24	0.82
19		224	185	0.83	0.775	0.020	0.096	0.0024	0.060	0.001	0.00	582	8	589	9	585	15	1.01
14		264	120	0.45	0.744	0.020	0.092	0.0024	0.059	0.001	0.06	564	8	567	10	564	18	1.00
69		39	33	0.84	0.687	0.022	0.089	0.0022	0.056	0.001	0.07	531	10	552	8	466	40	1.04
64		409	196	0.48	0.708	0.019	0.089	0.0021	0.058	0.001	0.02	544	8	549	7	531	15	1.01
56		37	66	1.77	0.693	0.026	0.089	0.0025	0.057	0.002	−0.24	534	13	548	10	494	49	1.02
52		113	49	0.44	0.720	0.022	0.088	0.0023	0.060	0.001	0.08	550	9	546	9	591	23	0.99
43		119	68	0.57	0.716	0.022	0.088	0.0025	0.059	0.001	−0.04	548	10	544	11	567	22	0.99
60	Core	148	95	0.64	0.708	0.019	0.087	0.0021	0.059	0.001	0.17	545	8	540	7	559	24	0.99
57		119	117	0.99	0.709	0.019	0.086	0.0024	0.059	0.001	0.20	544	7	532	10	574	24	0.98
62		456	176	0.39	0.691	0.018	0.086	0.0022	0.058	0.001	−0.01	535	8	532	8	539	12	1.00
27		61	45	0.74	0.681	0.023	0.086	0.0025	0.058	0.002	0.21	527	11	532	11	522	39	1.01
68		66	47	0.71	0.695	0.023	0.086	0.0023	0.058	0.001	0.04	535	11	531	9	558	33	0.99
42		136	114	0.84	0.692	0.020	0.086	0.0023	0.059	0.001	−0.12	534	9	530	9	551	24	0.99
13		184	64	0.35	0.674	0.017	0.085	0.0020	0.058	0.001	0.29	523	7	526	7	523	24	1.01
6		1215	931	0.77	0.694	0.016	0.085	0.0019	0.060	0.001	0.09	535	5	524	5	588	9	0.98
55		215	71	0.33	0.681	0.020	0.085	0.0021	0.058	0.001	−0.21	527	9	523	8	549	16	0.99
33		82	69	0.84	0.667	0.019	0.085	0.0025	0.058	0.001	0.10	519	9	523	10	512	26	1.01
12		74	55	0.75	0.656	0.018	0.084	0.0020	0.057	0.002	0.12	512	8	520	6	468	40	1.02
74	Core	48	38	0.78	0.675	0.021	0.084	0.0023	0.058	0.002	−0.04	524	10	519	9	520	42	0.99
34		296	229	0.77	0.655	0.017	0.083	0.0020	0.057	0.001	0.04	512	7	511	7	498	16	1.00
63		122	804	6.59	0.674	0.021	0.082	0.0022	0.059	0.001	−0.03	523	10	510	8	577	29	0.97
47		173	2	0.01	0.637	0.018	0.081	0.0019	0.058	0.001	−0.03	500	8	502	6	522	27	1.00
61	Rim	166	25	0.15	0.636	0.016	0.081	0.0020	0.057	0.001	0.25	500	6	502	7	481	18	1.00
7		763	40	0.05	0.761	0.021	0.080	0.0021	0.069	0.001	−0.49	575	8	497	8	903	13	0.86
67		394	4	0.01	0.635	0.015	0.079	0.0018	0.057	0.001	−0.15	499	5	493	6	500	14	0.99
75	Rim	222	5	0.02	0.625	0.017	0.079	0.0021	0.056	0.001	0.14	493	8	492	8	453	22	1.00
11		601	358	0.60	0.615	0.016	0.078	0.0020	0.057	0.001	0.02	487	6	486	7	501	13	1.00
26		125	103	0.82	0.604	0.015	0.078	0.0022	0.057	0.001	0.46	480	5	486	9	488	24	1.01
71		301	7	0.02	0.602	0.016	0.078	0.0020	0.056	0.001	0.18	478	6	482	7	453	19	1.01
29		261	11	0.04	0.685	0.082	0.077	0.0038	0.065	0.005	−0.90	524	46	479	21	740	140	0.90
10		393	91	0.23	0.582	0.016	0.075	0.0021	0.056	0.001	−0.13	465	7	468	8	463	14	1.00
53		253	8	0.03	0.581	0.017	0.075	0.0021	0.057	0.001	0.06	465	9	463	9	489	20	1.00
70		378	7	0.02	0.572	0.015	0.074	0.0019	0.055	0.001	0.11	459	7	458	8	434	17	1.00
17		337	12	0.03	0.535	0.013	0.072	0.0018	0.055	0.001	0.29	436	6	445	7	419	23	1.02
20		258	17	0.06	0.522	0.021	0.069	0.0027	0.055	0.001	−0.08	426	12	433	14	421	19	1.01
79		272	15	0.06	0.524	0.019	0.068	0.0023	0.056	0.001	−0.08	427	11	422	11	448	23	0.99
76		223	27	0.12	0.487	0.015	0.066	0.0018	0.054	0.001	−0.13	403	9	409	7	357	26	1.02
25		325	23	0.07	0.464	0.012	0.063	0.0016	0.053	0.001	0.10	387	5	396	6	352	14	1.02
59		989	54	0.05	0.474	0.012	0.062	0.0015	0.055	0.001	0.17	394	5	388	5	424	13	0.99
15		224	30	0.13	0.446	0.011	0.061	0.0014	0.053	0.001	0.06	375	5	380	4	337	22	1.01
36		1837	213	0.12	−0.001	0.000	0.000	0.0000	0.617	0.013	−0.46	−1	0	0	0	4547	6	0.08
8		937	352	0.38	−0.001	0.000	0.000	0.0000	0.576	0.012	−0.12	−1	0	0	0	4449	0	0.08

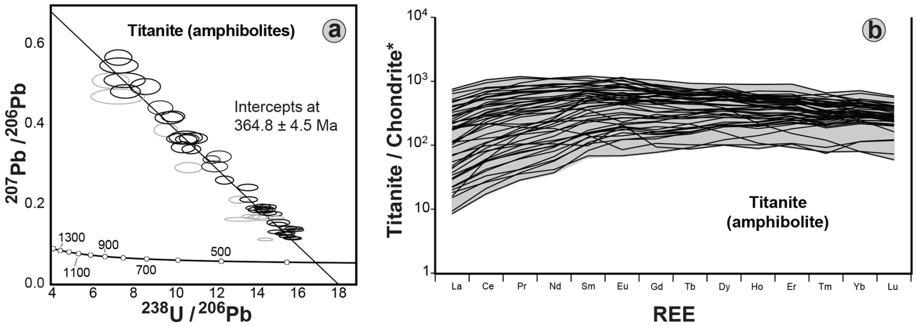

Figure 7. (a) Tera–Wasserburg diagram showing distribution of analyzed titanite ($n = 51$) from Sobrado amphibolite (JBP-71-21). The rejected analyses are represented by gray ellipses. The ellipses represent the $^{207}Pb/^{206}Pb$ and $^{238}U/^{206}Pb$ errors ($\pm 2\sigma$). **(b)** Chondrite-normalized REE patterns for the same titanite.

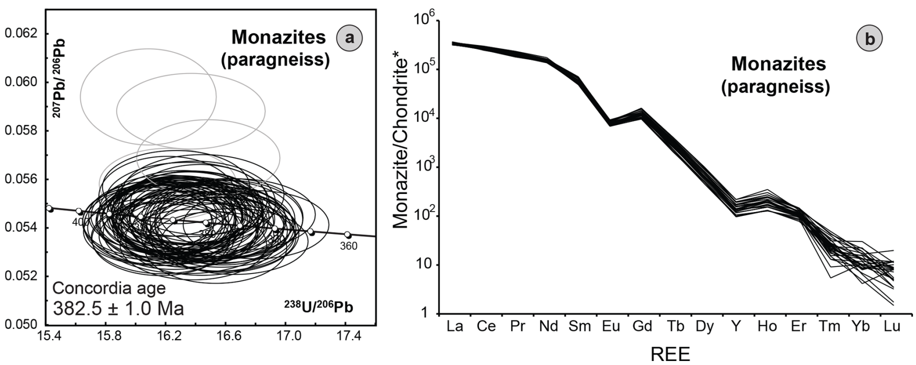

Figure 8. (a) Tera–Wasserburg diagram showing distribution of analyzed monazite ($n = 76$) from Sobrado paragneiss (JBP-71-15). The rejected analyses are represented by gray ellipses. The ellipses represent the $^{207}Pb/^{206}Pb$ and $^{238}U/^{206}Pb$ errors ($\pm 2\sigma$). **(b)** Chondrite-normalized REE patterns for the same monazite.

anomaly. The youngest ages (510–380 Ma) has a variable HREE slope, whereas the Eu anomaly is more regular, and the Ce anomaly is less marked.

When we plot age versus Hf, Yb/Gd and Eu/Ey* (Fig. 13a–c), the group of oldest ages (589–510 Ma) does not define any apparent trend. In sharp contrast, in the 500–380 Ma group it is remarkable not only the good correlation between age and composition but also the divergent evolution depending of the age (gray arrows). Hafnium, Yb/Gd and Eu/Eu* increase from 500 to ∼ 430 Ma, while there is a striking decrease from ∼ 420 to 380 Ma. Finally, we have used the U/Ce−Th graph proposed by Bacon et al. (2012) to discriminate between metamorphic and igneous zircon.

5 Discussion

5.1 Zircon geochronology: inheritance and age of magmatism

The presence of zircon inclusions shielded in garnets (e.g., Fig. 4e and g) is compatible with the preservation of magmatic, metamorphic or detrital inheritances during the syn-kinematic partial melting recorded in these rocks (Benítez Pérez, 2017). As shown in Fig. 12, the majority of analyzed zircon grains older than 600 Ma have fractionated REE patterns that are characteristic of igneous zircon (Hoskin and Schaltegger, 2003; Whitehouse and Platt, 2003; Hanchar and Westrenen, 2007; Grimes et al., 2015). Only three analyses show a flat HREE pattern that can be related to the presence of garnet and interpreted as metamorphic zircon. The provenance of these zircon grains older than 600 Ma in the Sobrado migmatitic paragneiss (Fig. 9b), is probably similar to those reported in the intermediate-P units of NW Spain upper allochthons like the Betanzos unit (Fuenlabrada et al., 2010) and Cariño gneiss (Albert et al., 2015). We obtained two Mesoproterozoic ages, between 1.2 and 1.4 Ga. Similar ages are also found in the parautochthonous (Díez Fernández et al., 2012), in the basal allochthonous units (Díez Fernández et al., 2010) and, to a lesser extent, in the intermediate-P units of NW Spain (Albert et al., 2015). These inherited zircons, although scarce (Fernández-Suárez et al., 2003), likely have their origin in rocks derived from Saharan and Arabian–Nubian cratons, and presumably transported during the Cadomian orogeny (e.g., Martínez Catalán et al., 2004). Paleoproterozoic populations range from 1.8 to 2.2 Ga, clustered at 2.1 Ga, are also common in the al-

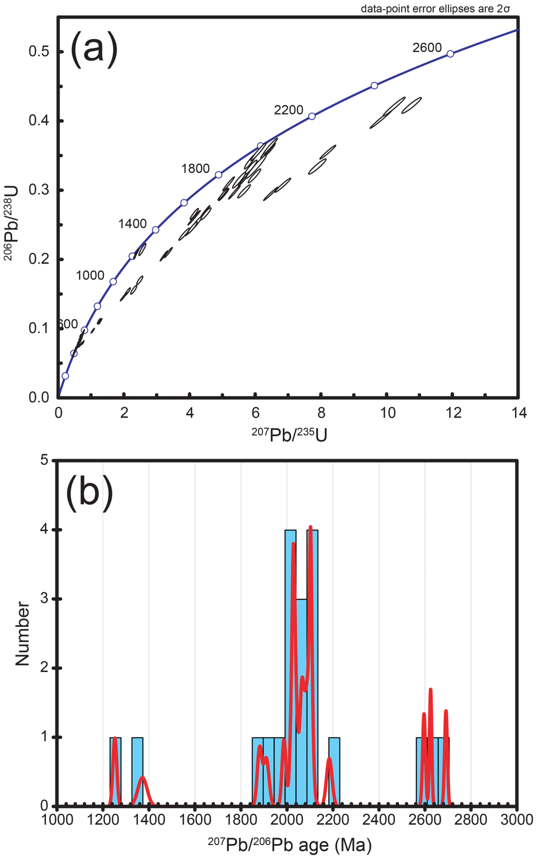

Figure 9. Concordia plot **(a)** including all zircon with concordance > 90 % from sample JBP-71-15 (Sobrado migmatitic paragneiss) and **(b)** age histogram and probability density plot for ages older than 1000 Ma.

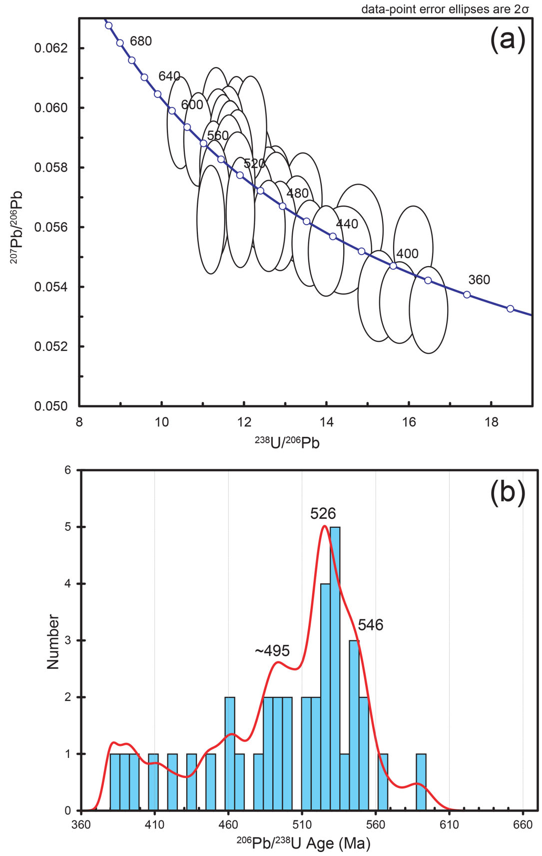

Figure 10. Tera–Wasserburg diagram **(a)** for the analyses between 589 and 380 Ma, and **(b)** age histogram and probability density plot for the same ages.

lochthonous complexes (Fernández-Suárez et al., 2003) and their origin likely involves materials generated or reworked during the Eburnean orogeny (e.g., Egal et al., 2002; Ennih and Liegeois, 2008) from the West African Craton (Peucat et al., 2005). Finally, the Archean population in the Sobrado paragneiss ranges from 2.5 to 2.8 Ga, and it is likely related to intrusive events in the western Reguibat Shield (Schofield et al., 2012) and the northern part of the West African Craton (Albert et al., 2015), with some reworking processes of juvenile rocks formed at approximately 3.0 Ga (Potrel et al., 1998).

Based on CL images, ages and zircon composition, we can determine that the youngest zircon with magmatic origin is grain number 34 (Fig. 6). The number obtained in this grain is comparable to other maximum depositional ages obtained from similar units in the NW Spain allochthonous complexes, such as the intermediate-P Betanzos uppermost unit (530–510 Ma; Fuenlabrada et al., 2010) and the intermediate-P Cariño uppermost unit (∼ 510 Ma; Albert et al., 2015).

In order to get more insight into the meaning of the data younger than 600 Ma, we have plotted these ages versus the

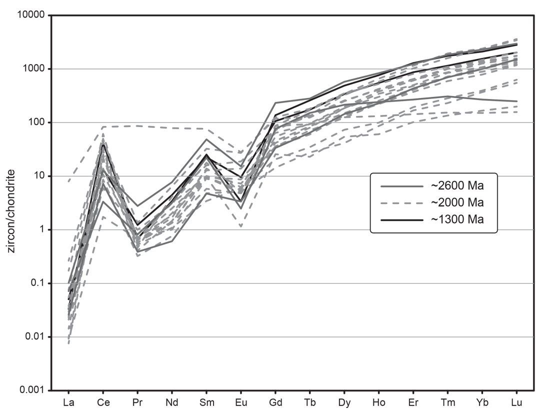

Figure 11. Chondrite-normalized plots for inherited zircon older than 1000 Ma.

Th/U ratios (Fig. 14). Analyses that yielded ages between 589 and 510 Ma cluster together with Th/U values higher than 0.3. The REE patterns displayed in this cluster are consistent with a magmatic origin. In the age versus Hf Yb/Gd and Eu/Eu* plots for this group (Fig. 13a–c), the absence of a trend suggests that the different zircon grains are not con-

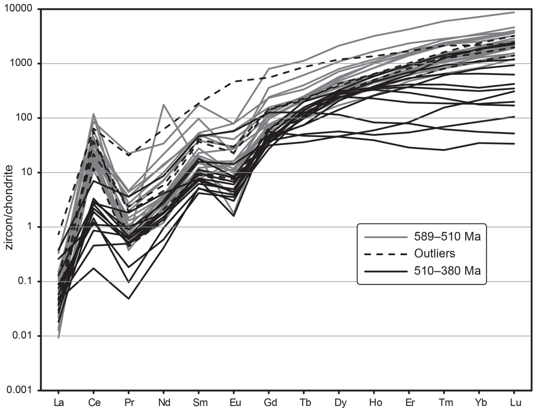

Figure 12. Chondrite-normalized plots for zircon between 589 and 380 Ma.

nected by a fractional crystallization process (e.g., Barth and Wooden, 2010). In the U/Ce−Th graph proposed by Bacon et al. (2012) to discriminate between metamorphic and igneous zircon, zircons with ages between 589 and 510 Ma are plotted in the igneous zircon field (Fig. 13d).

From the first group of data between 589 and 510 Ma, we can extract two ages: 546 ± 5 Ma out of six analyses, and 526 ± 3 Ma from 14 analyses (Fig. 15). These magmatic ages are also recognized in other well-characterized high-P/high-T units of the allochthonous complexes (Peucat et al., 1990; Santos Zalduegui et al., 2002; Castiñeiras et al., 2010), and they are related to a magmatic arc creation around the periphery of Gondwana (Abati et al., 1999, 2007).

5.2 Evolution of metamorphism of the Sobrado migmatitic paragneiss based on zircon composition

Extracting ages from a dataset where the data are evenly distributed from 500 to 380 Ma is a challenging task. When such smear in the age sorting happens, if we can rule out analytical error, we have three possibilities (e.g., Castiñeiras et al., 2010), namely (i) the correct age is the youngest and the dispersion is related to zircon inheritance, (ii) the real age is the oldest and the spread is caused by lead loss, or (iii) the age range is recording some kind of protracted geological event. Taking into account the CL texture of the youngest spots, we can remove the first possibility as the majority of analyses were performed in zircon rims. Furthermore, maximum depositional ages obtained from similar units from the allochthonous complexes preclude their interpretation as inheritance. The second possibility is plausible, considering the complex metamorphic evolution and the high grade attained by these rocks. However, a young lead loss episode should have affected also the inherited zircon ages, and the presence of various old age peaks (e.g., ∼ 2000, 546 and 536 Ma) suggests that they did not experienced lead loss. However, we can argue that limited lead loss occurred in some grains that have similar composition to the 589–510 Ma group ($Th/U > 0.15$) but younger ages (between 502 and 468 Ma). This group of outlier analyses (nos. 10, 11, 26 and 63) could have experienced a decoupling between their actual age and their composition (e.g., Flowers et al., 2012). Finally, we favor the last option when we take into account the strong correlation observed between age and zircon composition (Figs. 13a–c and 14).

This group of young analyses defines a trend with negative correlation from 500 to 380 Ma and Th/U values from 0.01 to 0.13. This correlation between the age and the composition of zircon suggests that the age dispersion is related to an actual geological process and is not caused by lead loss. Furthermore, even though the Th/U ratio shows a consistent evolution from 510 to 380 Ma, the rest of the proxies considered (Hf, Yb/Gd and Eu/Eu*, Fig. 13a–c) point to a two-stage evolution, and the characteristics of the REE patterns are compatible with a metamorphic origin (Chen et al., 2009, 2010; Rubatto et al., 2009; Peters et al., 2013; Stipska et al., 2016).

This scenario is congruent with the presence of two metamorphic events in the HP-HT units: one at ∼ 490–480 Ma and the other at ∼ 390–380 Ma (e.g., Fernández-Suárez et al., 2002, 2007). The increase in Yb/Gd values (Fig. 13b), related to the slope of the HREE, in zircons aged from 502 to 430 Ma is congruent with a higher availability of HREE in the rock. As garnet is the most important HREE reservoir in metamorphic rocks, we argue that this behavior is the record of the progressive destabilization of garnet in a decompressive path from HP-HT conditions. The increase observed in the Eu/Eu* ratio is consistent with a progressive destabilization of plagioclase, which is the main europium reservoir in rocks (Barth and Wooden, 2010; Castiñeiras et al., 2011).

The sharp decrease observed in the Yb/Gd ratio from 420 to 380 Ma is probably related to a new event of garnet growth (Rubatto et al., 2006; Stipska et al., 2016), i.e., the second HP-HT event. The evolution in the Eu/Eu* ratio suggests that this event took place under granulite facies conditions, as plagioclase was present to pump out all the available europium.

5.3 Monazite and titanite geochronology: age of the youngest metamorphism in the Sobrado antiform

The youngest zircon data recorded (380 ± 4 Ma) are consistent with the monazite concordia age (382 ± 1 Ma) in the migmatitic paragneiss of the middle tectonic slice. Besides, both monazite and irregular/subround zircons share their microtextural setting along the migmatitic fabric, pointing to a coeval character with partial melting at relatively high P. Furthermore, the chemical profiles observed in the monazite suggest simultaneous crystallization of this mineral with garnet (Rubatto, 2002; Rubatto et al., 2006; Mottram et al., 2014; Holder et al., 2015). Negative Eu anomalies indicate a preferential incorporation of europium to feldspars, in particular to K-feldspar, during melt crystallization (Buick et

Table 4. REE zircon_McD_S sorted by age.

Spot	Description	U (ppm)	Th (ppm)	Hf (ppm)	La (ppm)	Ce (ppm)	Pr (ppm)	Nd (ppm)	Sm (ppm)	Eu (ppm)	Gd (ppm)	Tb (ppm)	Dy (ppm)	Ho (ppm)	Er (ppm)	Tm (ppm)	Yb (ppm)	Lu (ppm)	Th/U	Yb/Gd	Eu/Eu*	Ce/Sm	Lu/Dy	U/Ce
8	c (h)	937	352	118 738	0.13	29.04	3.49	9.41	45.27	22.38	337	609	1451	2381	3575	4818	5839	6870	0.38	29.63	0.18	2.66	0.47	53
36	c (h)	1837	213	191 262	97.47	234.91	360.99	678.34	1304.05	710.48	980	590	691	934	1188	1866	2845	4106	0.12	0.61	0.63	0.75	0.59	13
15	r	224	30	113 786	0.04	3.33	0.67	3.06	17.91	8.35	56	47	46	39	29	26	35	34	0.13	0.71	0.26	0.77	0.07	110
59	c (h)	989	54	115 728	0.38	7.01	3.60	8.71	46.49	57.19	126	128	115	83	79	62	56	52	0.05	0.74	0.75	0.63	0.05	230
25	r	325	23	117 864	0.04	2.64	0.48	1.38	11.35	7.99	32	36	46	60	84	155	213	309	0.07	4.06	0.42	0.96	0.67	200
76	r	223	27	121 068	0.03	2.95	0.91	2.74	15.81	14.39	38	51	57	49	54	69	86	106	0.12	1.63	0.59	0.77	0.19	123
79	r	272	15	114 466	0.05	0.86	0.68	1.88	7.84	6.04	40	142	277	330	292	231	177	170	0.06	2.89	0.34	0.46	0.06	514
20	r	258	17	118 447	0.02	2.20	0.60	1.77	9.59	6.75	43	75	142	258	375	607	807	935	0.06	40.48	0.33	0.95	0.66	191
17	c (s)	337	12	126 214	0.06	1.89	0.52	1.53	6.22	4.97	46	74	208	383	625	1263	1870	2439	0.03	29.29	0.29	1.26	1.17	291
70	r	378	7	126 117	0.08	1.45	0.10	0.96	5.07	3.91	27	111	271	463	689	927	1093	1179	0.02	17.14	0.33	1.19	0.44	425
53	m	253	8	123 981	0.09	1.22	0.18	0.59	4.19	3.55	35	99	235	372	541	644	652	626	0.03	13.00	0.29	1.21	0.27	338
10	c (h)	393	91	104 563	0.03	57.59	0.64	2.12	9.05	6.75	66	122	283	504	813	1316	1764	2480	0.23	17.39	0.28	26.34	0.88	11
29	m	261	11	116 505	0.05	3.13	0.27	0.81	3.38	3.20	32	72	179	295	488	785	1075	1488	0.04	40.00	0.31	3.84	0.83	136
71	r	301	7	123 204	0.13	2.76	1.83	4.16	7.64	4.44	35	136	326	582	938	1433	1820	2276	0.02	27.14	0.27	1.50	0.70	178
26	c (s)	125	103	94 660	0.13	21.86	2.38	5.86	41.08	29.66	146	227	393	625	901	1239	1553	1976	0.82	6.39	0.38	2.20	0.50	9
11	c (h)	601	358	131 456	0.05	36.87	1.93	4.60	36.89	23.09	143	211	427	647	1019	1615	2373	3215	0.60	4.89	0.32	4.14	0.75	27
7	c (b)	763	40	131 553	0.87	9.15	10.13	11.36	28.78	28.60	106	165	404	661	1075	1822	2658	3374	0.05	9.80	0.52	1.32	0.83	136
67	c (h)	394	4	122 330	0.05	0.46	0.50	1.86	7.50	1.60	60	199	313	348	369	340	314	350	0.01	15.00	0.08	0.25	0.11	1407
75	c (o)	222	5	119 417	0.26	1.11	1.01	1.77	7.09	4.44	48	157	299	366	412	413	360	423	0.02	7.65	0.24	0.65	0.14	326
47	m	173	2	120 291	0.05	0.17	0.05	0.42	5.20	3.02	43	124	247	229	193	186	182	199	0.01	8.67	0.20	0.14	0.08	1619
61	c (h)	166	25	100 291	0.05	12.07	0.44	1.31	10.07	7.46	46	106	241	366	534	806	1118	1398	0.15	5.52	0.35	4.97	0.58	22
63	c (h)	122	804	22 524	0.74	64.11	20.58	62.36	185.81	467.14	553	861	1191	1363	1688	2126	2193	2309	6.59	1.11	1.46	1.43	0.19	3
34	o	296	229	109 515	0.06	112.07	0.55	2.19	18.51	10.48	116	249	524	1007	1506	2324	2969	3943	0.77	24.81	0.23	25.07	0.75	4
74	m	48	38	92 427	0.08	14.71	0.56	1.53	7.57	16.16	56	121	267	445	749	1255	1503	2114	0.78	9.09	0.79	8.05	0.79	5
12	o	74	55	84175	0.05	19.90	1.48	3.63	20.34	11.90	75	112	241	443	608	915	1286	1537	0.75	7.50	0.30	4.05	0.64	6
55	c (o)	215	71	99 515	0.04	16.66	0.60	175.05	14.73	10.83	67	152	303	496	875	1215	1553	2130	0.33	12.92	0.34	4.68	0.70	21
6	c (o)	1215	931	83 883	0.33	85.32	22.41	34.14	175.00	78.51	799	1127	2130	3205	4256	5980	7205	8699	0.77	12.47	0.21	2.02	0.41	23
33	o	82	69	77 184	0.13	57.10	2.70	10.09	53.31	79.40	234	335	715	1081	1769	2725	3534	4634	0.84	7.16	0.71	4.44	0.65	2
13	c (o)	184	64	96 602	0.01	14.68	0.51	1.20	11.08	8.88	72	122	262	467	719	1053	1360	1923	0.35	10.56	0.31	5.49	0.73	20
42	c (o)	136	114	70 291	0.15	26.59	3.59	14.22	44.26	58.97	157	235	382	641	950	1547	2000	2642	0.84	6.67	0.71	2.49	0.69	8
68	c (o)	66	47	93 981	0.07	23.00	0.38	2.41	8.65	11.55	39	97	172	262	478	652	842	1224	0.71	4.69	0.63	11.02	0.71	5
57	c (o)	119	117	74 175	0.11	33.77	4.64	21.88	97.30	22.02	360	615	1085	1676	2350	2862	3385	3817	0.99	23.91	0.12	1.44	0.35	6
27	c (s)	61	45	90 097	0.01	21.40	0.59	2.67	10.47	8.70	71	103	213	352	523	814	1056	1411	0.74	6.25	0.32	8.46	0.66	5
62	c (o)	456	176	98 058	0.05	21.70	2.33	7.26	38.45	30.02	108	202	365	588	962	1421	2087	2907	0.39	4.62	0.47	2.34	0.80	34
60	m	148	95	93 107	0.12	31.32	4.38	13.37	50.68	41.03	130	248	442	617	906	1360	1646	2150	0.64	6.22	0.51	2.56	0.49	8
43	c (o)	119	68	84 466	0.05	11.00	0.75	3.94	22.77	27.18	77	152	326	496	773	1202	1559	2053	0.57	6.25	0.65	2.00	0.63	18
52	c (o)	113	49	110 874	0.02	36.87	0.55	2.10	15.68	16.16	95	217	480	830	1400	2117	2944	4024	0.44	9.09	0.42	9.74	0.84	5
56	c (s)	37	66	90 971	0.09	118.60	1.95	7.07	49.66	27.53	242	402	793	1201	1756	2275	2522	3256	1.77	13.41	0.25	9.89	0.41	1
64	c (o)	409	196	122 136	0.05	45.35	0.86	3.41	20.27	1.78	101	224	480	835	1513	2275	2783	3638	0.48	30.00	0.04	9.27	0.76	15
69	c (h)	39	33	100 583	0.01	19.90	0.66	1.82	12.16	14.03	57	121	226	374	623	834	1118	1553	0.84	5.25	0.53	6.78	0.69	3
14	c (h)	264	120	108 835	0.01	27.08	1.31	2.47	11.35	3.91	72	116	253	449	688	1113	1404	1955	0.45	13.85	0.14	9.88	0.77	16
73	r	238	34	114 369	0.09	10.28	1.86	4.97	21.62	15.81	75	189	289	447	575	810	901	1150	0.14	6.36	0.39	1.97	0.40	38
19	o	224	185	100 388	0.02	38.34	1.07	3.89	27.91	9.77	136	252	569	1004	1563	2413	3019	3813	0.83	34.50	0.16	5.69	0.67	10
77	m	397	18	123 301	0.38	3.07	1.47	3.00	19.12	12.43	74	158	205	203	248	331	400	423	0.05	2.48	0.33	0.66	0.21	211
78	r	157	40	85 631	0.18	11.75	1.50	1.95	6.01	11.19	28	53	89	121	238	416	573	907	0.26	3.62	0.86	8.09	1.02	22
30	r (o)	270	29	111 068	0.04	4.26	0.24	0.94	6.15	6.22	55	120	256	410	628	955	1137	1402	0.11	13.53	0.34	2.87	0.55	103
45	c (s)	65	29	100 971	0.05	7.94	0.17	1.05	9.32	8.35	26	66	132	194	333	474	609	793	0.45	6.19	0.54	3.53	0.60	13
41	c (h)	36	16	94 660	0.03	15.01	0.44	1.55	7.09	9.77	47	71	138	225	406	619	814	1061	0.45	8.64	0.53	8.76	0.77	4
9	o	53	45	82 718	0.03	35.73	1.76	4.99	21.35	13.68	101	129	269	434	559	789	1106	1358	0.84	7.62	0.30	6.93	0.50	2
50	c (o)	321	114	97 087	0.38	18.76	0.80	3.74	14.46	18.29	59	108	226	379	621	976	1205	1565	0.35	8.21	0.62	5.37	0.69	28
58	c (o)	463	39	113 010	0.30	4.32	1.37	2.47	15.54	14.92	59	124	200	273	375	502	632	850	0.08	2.94	0.49	1.15	0.43	175
46	c (h)	275	126	105 825	0.03	41.60	0.69	3.44	25.34	3.37	137	260	488	766	1288	1753	2112	2817	0.46	23.13	0.06	6.80	0.58	11
38	c (o)	48	27	84 078	0.05	13.51	1.23	4.46	22.50	9.59	107	174	341	549	869	1150	1547	2033	0.56	10.87	0.20	2.49	0.60	6
31	m	41	17	108 350	0.04	15.50	0.22	0.83	6.08	4.97	13	29	51	104	181	307	492	720	0.41	6.40	0.57	10.56	1.40	4
22	c (h)	128	32	95 728	0.01	1.75	0.68	2.52	9.59	1.15	26	23	54	61	102	136	167	199	0.25	8.14	0.07	0.75	0.37	119
24	c (h)	166	71	117 573	0.02	6.04	1.00	3.04	17.91	4.97	86	94	126	132	143	153	151	157	0.43	2.56	0.13	1.40	0.12	45
65	c (s)	407	6	124 078	0.02	0.44	0.29	0.88	13.58	2.13	89	216	261	218	201	213	239	239	0.02	3.55	0.06	0.13	0.09	1508
81	c (o)	80	47	79 709	0.08	24.96	0.89	2.54	12.97	32.68	65	158	296	542	1025	1615	2348	3687	0.59	5.96	1.12	7.97	1.25	5
23	c (o)	71	51	90 291	0.03	28.71	1.33	3.92	19.26	15.45	84	120	221	368	566	818	1236	1602	0.71	6.92	0.38	6.18	0.72	4
54	m	66	43	97 379	0.31	22.51	0.82	3.79	16.28	10.48	76	125	205	344	533	794	981	1329	0.64	5.45	0.30	5.73	0.65	5
39	c (o)	125	113	92 039	0.08	61.34	0.46	4.16	15.95	18.83	75	134	259	408	631	866	1261	1565	0.90	6.67	0.54	15.93	0.60	3
1	c (s)	52	36	89 126	22.83	74.39	75.75	54.05	50.00	16.87	84	97	213	346	534	798	1186	1602	0.70	6.25	0.26	6.16	0.75	1
44	c (o)	100	109	83 786	0.17	44.05	1.35	6.46	32.43	27.18	125	182	351	526	813	1097	1385	1772	1.09	5.43	0.43	5.63	0.50	4
21	o	587	251	110 194	0.04	20.39	0.71	1.88	9.59	5.51	54	96	198	379	609	1000	1311	1748	0.43	10.40	0.24	8.80	0.88	47
16	c (o)	118	107	98 835	8.02	83.20	86.21	78.77	76.35	27.89	118	124	251	425	650	1016	1478	2028	0.91	4.09	0.29	4.51	0.81	2
5	m	70	102	97 767	0.01	25.61	0.58	1.33	5.81	4.80	36	60	136	222	373	595	786	1183	1.47	9.33	0.33	18.26	0.87	4
83	c (s)	48	22	81 942	0.02	8.65	0.32	0.77	4.80	5.15	14	28	41	86	168	232	370	549	0.47	4.41	0.62	7.46	1.32	9
80	c (s)	46	34	98 738	0.04	30.67	0.41	1.47	9.66	8.70	46	85	150	256	424	725	888	1240	0.74	7.08	0.41	13.15	0.83	2
32	o	101	49	103 010	0.27	49.92	0.69	3.15	10.07	7.28	36	71	123	229	406	704	1075	1488	0.49	13.75	0.38	20.54	1.21	3
40	m (s)	62	40	89 709	0.02	34.26	0.56	2.04	12.84	13.85	64	94	185	302	483	704	1025	1329	0.64	3.87	0.48	11.05	0.72	3
48	c (s)	28	15	91 553	0.03	13.88	0.53	1.09	3.45	6.04	21	35	74	100	194	285	395	630	0.53	3.15	0.72	16.69	0.86	3
4	c (h)	677	299	110 194	0.01	21.04	0.66	1.40	9.59	4.80	72	140	327	579	1025	1595	2329	3443	0.44	32.31	0.18	9.08	1.05	52
37	c (s)	151	53	94 951	0.01	22.02	0.64	1.68	13.85	6.22	87	170	343	661	1150	1947	2391	3610	0.35	13.85	0.18	6.59	1.05	11
51	c (o)	304	97	107 767	0.21	6.82	0.72	2.76	16.96	3.91	71	145	273	480	800	1089	1509	2167	0.32	17.65	0.11	1.67	0.79	73
18	c (o)	49	19	91 553	0.05	10.77	0.73	1.01	9.12	5.51	42	80	186	344	500	846	1081	1439	0.38	17.33	0.28	4.89	0.77	7
35	o	182	124	99 515	0.08	3.38	0.53	2.54	13.31	4.09	68	98	170	260	328	478	522	679	0.68	10.00	0.14	1.05	0.40	88
66	c (o)	693	223	106 699	0.23	16.97	1.29	4.75	17.16	44.23	59	116	204	352	580	781	1081	1411	0.32	2.17	1.39	4.09	0.69	67
49	c (o)	403	115	125 922	0.11	2.28	0.54	2.01	20.07	1.74	93	161	232	251	306	348	337	386	0.29	11.58	0.04	0.47	0.17	288
2	r	444	141	105 728	0.09	8.40	1.38	2.54	15.68	7.82	90	129	267	425	611	899	1118	1610	0.32	8.18	0.21	2.22	0.60	86
28	c (h)	878	74	98 350	0.48	11.97	4.04	6.48	16.82	8.88	35	61	97	171	259	445	646	878	0.08	7.78	0.37	2.95	0.90	120
72	r	495	22	110 194	0.03	7.26	0.39	0.61	4.73	3.37	34	65	145	229	432	700	994	1504	0.04	16.92	0.27	6.36	1.04	111
82	c (b)	280	136	129 029	0.07	3.34	0.82	3.22	22.16	2.49	76	151	215	242	269	308	269	250	0.48	9.17	0.06	0.63	0.12	137
3	c (h)	690	223	96 505	0.10	12.72	2.78	7.72	48.58	15.28	233	280	577	837	1231	1846	2304	2959	0.32	10.91	0.14	1.08	0.51	88

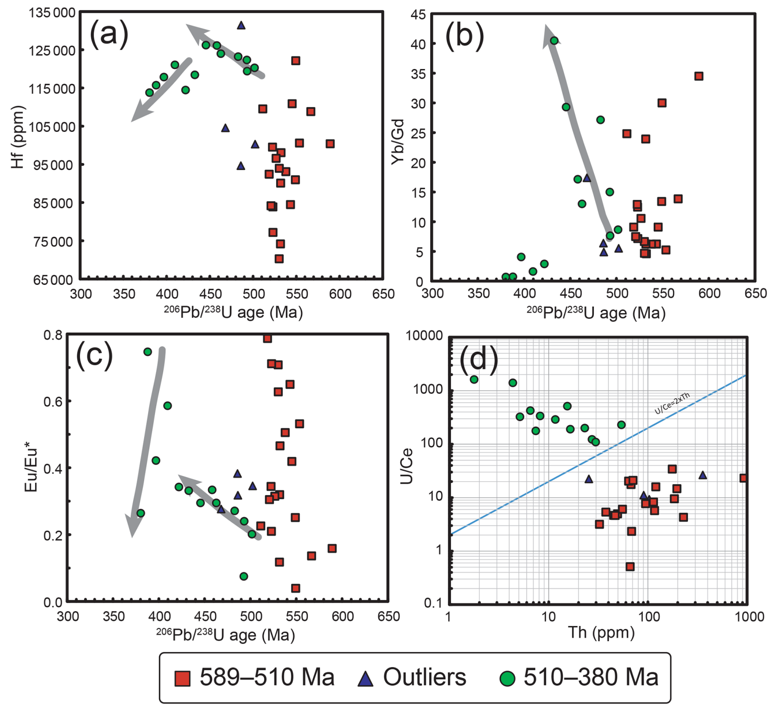

Figure 13. **(a)** Hafnium versus age, **(b)** Yb/Gd versus age, **(c)** Eu/Eu* versus age and **(d)** U/Ce versus Th for zircon analyses between 589 and 380 Ma.

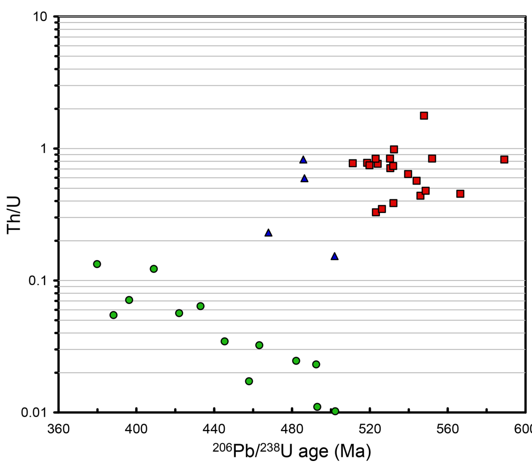

Figure 14. Th/U ratio versus ^{206}Pb/^{238}U ages for the zircon analyses from 589 to 380 Ma. Analysis 63 (510 Ma) is not represented as it has an anomalous value (6.59).

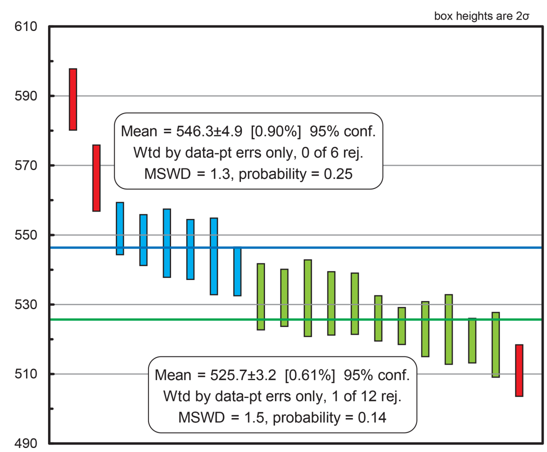

Figure 15. Weighted average obtained from magmatic ages distributed between 589 and 510 Ma.

al., 2010; Rubatto et al., 2013). These characteristics are compatible with monazite crystallization in a single pulse (MSWD < 1) in the presence of garnet, supporting its metamorphic origin. This Middle Devonian age can be interpreted to represent the minimum age of the youngest metamorphic event in the Sobrado unit, which reached high-P granulite facies (Fernández-Suárez et al., 2007; Ordóñez Casado et al., 2001). It is suggested that monazite captures the onset of the exhumation process in the migmatitic paragneiss (Holder et al., 2015).

Titanite crystallization is syn-kinematic with the mylonitic fabric of the fine-grained amphibolites located at the base of the upper tectonic slice. The growth of titanite in amphibolitic conditions is supported by the umbrella-shaped REE patterns shown in Fig. 7b, typical of titanite coexisting with amphibole (Mulrooney and Rivers, 2005; Chambefort et al., 2013; Lesnov, 2013). A Late Devonian age (∼ 365 Ma) could be related to the onset of retrograde metamorphic condi-

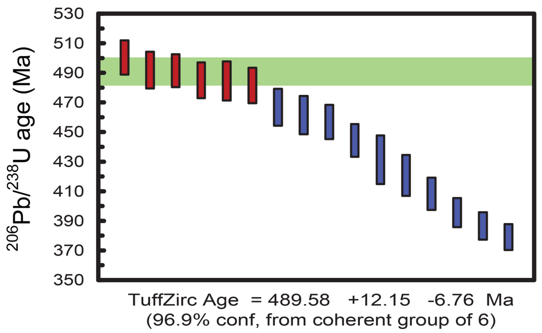

Figure 16. Age of the onset of the oldest HP-HT metamorphic event obtained using the TuffZirc algorithm.

tions during the development of the shear zone and suggests a prolongated exhumation process reaching amphibolite facies. The Late Devonian age lies close to the Ar–Ar exhumation ages of the uppermost units in the Órdenes Complex as recorded in the Corredoiras detachment (376 ± 2.0 Ma in hornblende; Dallmeyer et al., 1997), or in the Ponte Carreira Detachment (371 ± 4.0 Ma in muscovite; Gómez Barreiro et al. 2006).

The U–Pb zircon age for the onset of the oldest metamorphic event was estimated using the TuffZirc method, developed by Ludwig and Mundil (2002), which calculates the median by choosing the largest set of concordant analyses that are statistically coherent. The best estimate obtained for this event is 489.58 (+12.15–6.76) Ma, obtained by pooling together only six of 16 analyses (Fig. 16). The 510–380 Ma zircon aliquot shows a clear correlation between its cathodoluminescence texture and its geochemistry and could be also related to shielded population of "metamorphic" zircon grains within garnets (Fig. 4e). The age recorded in the migmatitic paragneiss is thought to correspond to a metamorphic event, dated in the Early Ordovician (∼ 490 Ma) and is in very good agreement with upper high-P/high-T dates of equivalent units carried out during previous studies (Kuijper, 1979; Peucat et al., 1990; Fernández-Suárez et al., 2002, 2007). This age also coincides with those obtained from intermediate-P units, where large plutons were emplaced and there is a lack of later high-P/high-T metamorphism during the Devonian. The westernmost upper intermediate-P units of the Órdenes Complex underwent a granulite facies metamorphism dated between approximately 500 and 485 Ma, contemporaneous with the intrusion of massive gabbros and granodiorites related to Cambrian magmatic arc activity (Abati et al., 1999, 2003, 2007; Andonaegui et al., 2002, 2012, 2016; Castiñeiras et al., 2002, 2010). The granulite facies metamorphism is associated with heating produced by the intrusions, accompanied by a quick burial, almost coeval with igneous emplacement (Abati et al., 2003; Castiñeiras, 2005; Fernández-Suárez et al., 2007).

Clearly, the metamorphic event recorded in some zircons is pre-Variscan, and it is therefore independent of the high-P/high-T granulite facies metamorphism that occurred during the Early–Middle Devonian that has been identified in the underlying upper units, such as in Sobrado with 660–770 °C and 13–17 kbar (Arenas and Martínez Catalán, 2002) or 750–850 °C and 12–15 kbar (Benítez-Pérez, 2017). The pre-Variscan metamorphism was probably followed by a decompression stage, associated with partial melting (Fernández-Suárez et al., 2002). Later on, HP-HT Devonian metamorphism occurred, during which exhumation through an isothermal decompression led to partial melting in paragneiss and basic granulites (Fernández-Suárez et al., 2007). As the zircon composition and microstructural setting clearly suggest, the notable slope observed in the TuffZirc plot from 489 to 380 Ma (Fig. 16) is the result of these exhumation, burial and new exhumation processes accompanied by partial melting, in which the shielding role of garnet has been important.

6 Conclusions

This study provides new age constraints on the processes that have affected the Sobrado unit, part of the Órdenes Complex, and allows some correlation with events recognized in other parts of the allochthonous high-P/high-T complexes of NW Spain. Titanite, monazite and zircon dating together with REE analyses have been combined together in these rocks for the first time in order to carry out a geochronological investigation of the amphibolites and paragneiss.

According to the analyses, the youngest ages recorded by the metamorphic zircons are consistent with the concordia monazite age obtained from 76 analyses in the paragneiss. The microtextural setting of both metamorphic zircon and monazite along the HP-HT main foliation support that interpretation. Therefore, the Middle Devonian age (∼ 380 Ma) represents the minimum age of the last Sobrado metamorphic event under high-P granulite facies conditions and represents the first stages of the Variscan orogeny in this part of Spain. Dating of metamorphic titanite in the amphibolite yields a Late Devonian age (∼ 365 Ma) and is associated with very homogeneous REE patterns suggesting the prolongation of the exhumation process in the Sobrado unit, reaching amphibolite facies metamorphic conditions. In zircon, there is a strong relationship between their textures, as seen in cathodoluminescence images, REE patterns and $^{206}Pb/^{238}U$ ages. Metamorphic zircon defines an Early Ordovician age (∼ 490 Ma) although it shows a large dispersion. This date is linked to the first pre-Variscan granulite facies metamorphism seen in the Sobrado unit under intermediate-P conditions, and it is interpreted to be related to the intrusion of basic and intermediate composition rocks, and coeval with burial in a magmatic arc context. Microstructural analysis of zircon, monazite and titanite provide complementary microtextural context to understand the origin of this population mixture. In situ dating should be conducted to confirm some textural relationships in the future.

The maximum depositional age of the Sobrado unit is suggested to be late Cambrian based on the age of the youngest inherited zircon (511 Ma). From the youngest set of inherited zircon, two ages can be obtained (546 and 526 Ma), pointing to the formation of a peri-Gondwanan magmatic arc. The protoliths of inherited zircon older than 1000 Ma from the Sobrado unit are found in other Spanish complexes and are thought to be related to sources mainly in the West African Craton.

Data availability. The data are not publicly accessible.

Author contributions. JMBP, PC, JGB and JRMC contributed equally to the fieldwork, experimental process and elaboration of the manuscript. AKC contributed to U–Pb–REE acquisition and data reduction, and RH participated in the writing of the text and the geological interpretation.

Competing interests. The authors declare that they have no conflict of interest.

Acknowledgements. We kindly appreciate excellent reviews from Michele Zucali, Federico Rossetti, Puy Ayarza and an anonymous referee which contributed to improving the manuscript.

Financial support. This research has been supported by the Spanish Ministry of Economy, Industry and Competitiveness (grant no. CGL2016-78560-P), the Spanish Ministry of Economy, Industry and Competitiveness (grant no. CGL2011-22728), the Spanish Ministry of Science and Innovation (grant no. IEDI-2016-00691) and the Spanish Ministry of Economy, Industry and Competitiveness (grant no. FPI 2013-2016 (BES-2012-059893)).

Review statement. This paper was edited by Federico Rossetti and reviewed by Michele Zucali and one anonymous referee.

References

Abati, J., Dunning, G. R., Arenas, R., Díaz García, F., González Cuadra, P., Martínez Catalán, J. R., and Andonaegui, P.: Early Ordovician orogenic event in Galicia (NW Spain): Evidence from U-Pb ages in the uppermost unit of the Ordenes Complex, Earth Planet. Sc. Lett., 165, 213–228, https://doi.org/10.1016/S0012-821X(98)00268-4, 1999.

Abati, J., Arenas, R., Martinez Catalán, J. R., and Díaz García, F.: Anticlockwise P-T Path of Granulites from the Monte Castelo Gabbro (Ordenes Complex, NW Spain), J. Petrol., 44, 305–327, https://doi.org/10.1093/petrology/44.2.305, 2003.

Abati, J., Castiñeiras, P., Arenas, R., Fernández-Suárez, J., Barreiro, J. G., and Wooden, J. L.: Using SHRIMP zircon dating to unravel tectonothermal events in arc environments. The early Palaeozoic arc of NW Iberia revisited, Terra Nova, 19, 432–439, https://doi.org/10.1111/j.1365-3121.2007.00768.x, 2007.

Abati, J., Gerdes, A., Suárez, J. F., Arenas, R., Whitehouse, M. J., and Fernández, R. D.: Magmatism and early-Variscan continental subduction in the northern Gondwana margin recorded in zircons from the basal units of Galicia, NW Spain, Bull. Geol. Soc. Am., 122, 219–235, https://doi.org/10.1130/B26572.1, 2010.

Aerden, D. G. A. M.: Correlating deformation in Variscan NW-Iberia using porphyroblasts; implications for the Ibero-Armorican Arc, J. Struct. Geol., 26, 177–196, https://doi.org/10.1016/S0191-8141(03)00070-1, 2004.

Albert, R., Arenas, R., Gerdes, A., Sánchez-Martínez, S., Fernández-Suárez, J., and Fuenlabrada, J. M.: Provenance of the Variscan Upper Allochthon (Cabo Ortegal Complex, NW Iberian Massif), Gondwana Res., 28, 1434–1448, https://doi.org/10.1016/j.gr.2014.10.016, 2015.

Aleinikoff, J. N., Schenck, W. S., Plank, M. O., Srogi, L. A., Fanning, C. M., Kamo, S. L., and Bosbyshell, H.: Deciphering igneous and metamorphic events in high-grade rocks of the Wilmington complex, Delaware: Morphology, cathodoluminescence and backscattered electron zoning, and SHRIMP U-Pb geochronology of zircon and monazite, Bull. Geol. Soc. Am., 118, 39–64, https://doi.org/10.1130/B25659.1, 2006.

Aleinikoff, J. N., Wintsch, R. P., Tollo, R. P., Unruh, D. M., Fanning, C. M., and Schmitz, M. D.: Ages and origins of rocks of the Killingworth dome, south-central Connecticut: Implications for the tectonic evolution of southern New England, Am. J. Sci., 307, 63–118, https://doi.org/10.2475/01.2007.04, 2007.

Alvarez-Valero, A. M., Gómez-Barreiro, J., Alampi, A., Castineiras, P., and Martinez Catalán, J. R.: Local isobaric heating above an extensional detachment in the middle crust of a Variscan allochthonous terrane (Ordenes complex, NW Spain), Lithosphere-US, 6, 409–418, https://doi.org/10.1130/L369.1, 2014.

Andonaegui, P., Castiñeiras, P., González Cuadra, P., Arenas, R., Sánchez Martínez, S., Abati, J., Díaz García, F., and Martínez Catalán, J. R.: The Corredoiras orthogneiss (NW Iberian Massif): Geochemistry and geochronology of the Paleozoic magmatic suite developed in a peri-Gondwanan arc, Lithos, 128–131, 84–99, https://doi.org/10.1016/j.lithos.2011.11.005, 2012.

Andonaegui, P., González Del Tánago, J., Arenas, R., Abati, J., Martínez Catalán, J. R., Peinado, M., and Díaz García, F.: Tectonic setting of the Monte Castelo gabbro (Ordenes Complex, northwestern Iberian Massif): Evidence for an arc-related terrane in the hanging wall to the Variscan suture, Geol. S. Am. S., 364, 37–56, https://doi.org/10.1130/0-8137-2364-7.37, 2002.

Andonaegui, P., Sánchez-Martínez, S., Castiñeiras, P., Abati, J., and Arenas, R.: Reconstructing subduction polarity through the geochemistry of mafic rocks in a Cambrian magmatic arc along the Gondwana margin (Órdenes Complex, NW Iberian Massif), Int. J. Earth Sci., 105, 713–725, https://doi.org/10.1007/s00531-015-1195-x, 2016.

Arenas, R., and Martínez Catalán, J. L.: Prograde development of corona textures in metagabbros of the Sobrado unit (Órdenes Complex, northwestern Iberian Massif): Variscan-Appalachian dynamics: The building of the late Paleozoic basement, Special Papers Geological Society of America, 364, 73–88, https://doi.org/10.1130/0-8137-2364-7.73, 2002.

Bacon, C. R., Vazquez, J. A., and Wooden, J. L.: Peninsular terrane basement ages recorded by Paleozoic and Paleoproterozoic zircon in gabbro xenoliths and andesite from Redoubt volcano, Alaska, Bull. Geol. Soc. Am., 124, 24–34, https://doi.org/10.1130/B30439.1, 2012.

Ballèvre, M., Martínez Catalán J. R., López-Carmona, A., Pitra, P., Abati, J., Díez Fernández, R., Ducassou, C., Arenas, R., Bosse, V., Castiñeiras, P., Fernández-Suárez, J., Gómez Barreiro, J., Paquette, J.-L., Peucat, J.-J., Poujol, M., Ruffet, G., and Sánchez Martínez, S.: Correlation of the nappe stack in the Ibero-Armorican arc across the Bay of Biscay: a joint French–Spanish project, Geological Society, London, Special Publications, 405, 77–113, https://doi.org/10.1144/SP405.13, 2014.

Barth, A. P. and Wooden, J. L.: Coupled elemental and isotopic analyses of polygenetic zircons from granitic rocks by ion microprobe, with implications for melt evolution and the sources of granitic magmas, Chem. Geol., 277, 149–159, https://doi.org/10.1016/j.chemgeo.2010.07.017, 2010.

Belousova, E. A., Griffin, W. L., O'Reilly, S. Y., and Fisher, N. I.: Igneous zircon: trace element composition as an indicator of source rock type, Contrib. Mineral. Petr., 143, 602–622, https://doi.org/10.1007/s00410-002-0364-7, 2002.

Benítez-Pérez, J. M.: Quantitative study of texture in tectonites by diffraction. Contribution to seismic anisotropy and orogenic rheology, PhD. Thesis, University of Salamanca, Spain, 2017.

Buick, I. S., Clark, C., Rubatto, D., Hermann, J., Pandit, M., and Hand, M.: Constraints on the Proterozoic evolution of the Aravalli-Delhi Orogenic belt (NW India) from monazite geochronology and mineral trace element geochemistry, Lithos, 120, 511–528, https://doi.org/10.1016/j.lithos.2010.09.011, 2010.

Castiñeiras, P., Andonaegui, P., Arenas, R., and Martinez Catalán, J.: Descripción y resultados preliminares del plutón compuesto de San Xiao, Complejo de Cabo Ortegal (noroeste del Macizo Ibérico), Geogaceta, 32, 111–114, 2002.

Castiñeiras, P.: Origen y evolución tectonotermal de las unidades de O Pino y Cariño (Complejos Alóctonos de Galicia), Laboratorio Xeolóxico de Laxe, Serie Nova Terra, 28, A Coruña., 2005.

Castiñeiras, P., García, F. D., and Gómez-Barreiro, J.: REE-assisted U-Pb zircon age (SHRIMP) of an anatectic granodiorite: Constraints on the evolution of the A Silva granodiorite, Iberian allochthonous complexes, Lithos, 116, 153–166, https://doi.org/10.1016/j.lithos.2010.01.013, 2010.

Castiñeiras, P., Navidad, M., Casas, J. M., Liesa, M., and Carreras, J.: Petrogenesis of Ordovician Magmatism in the Pyrenees (Albera and Canigó Massifs) Determined on the Basis of Zircon Minor and Trace Element Composition, J. Geol., 119, 521–534, https://doi.org/10.1086/660889, 2011.

Chen, R. X., Zheng, Y. F., and Xie, L.: Metamorphic growth and recrystallization of zircon: Distinction by simultaneous in-situ analyses of trace elements, U-Th-Pb and Lu-Hf isotopes in zircons from eclogite-facies rocks in the Sulu orogen, Lithos, 114, 132–154, https://doi.org/10.1016/j.lithos.2009.08.006, 2010.

Cheng, H., King, R. L., Nakamura, E., Vervoort, J. D., Zheng, Y. F., Ota, T., Wu, Y. B., Kobayashi, K., and Zhou, Z. Y.: Transitional time of oceanic to continental subduction in the Dabie orogen: Constraints from U-Pb, Lu-Hf, Sm-Nd and Ar-Ar multichronometric dating, Lithos, 110, 327–342. https://doi.org/10.1016/j.lithos.2009.01.013, 2009.

Cherniak, D. J.: Zr diffusion in titanite, Contrib. Mineral. Petr., 152, 639–647, https://doi.org/10.1007/s00410-006-0133-0, 2006.

Corfu, F., Hanchar, J. M., Hoskin, P. W. O., and Kinny, P. D.: Atlas of Zircon Textures, in: Zircon. Reviews in Mineralogy and Geochemistry, edited by: Hanchar, J. M. and Hoskin, P. W. O. Mineralogical Society of America, 468–500, 2003.

Corrie, S. L. and Kohn, M. J.: Trace-element distributions in silicates during prograde metamorphic reactions?: implications for monazite formation, Journal of Metamorphic Geology, 26, 451–464, https://doi.org/10.1111/j.1525-1314.2008.00769.x, 2008.

Dallmeyer, R. D., Martínez Catalán, J. R., Arenas, R., Gil Ibarguchi, J. I., Gutiérrez-Alonso, G., Farias, P., Bastida, F., and Aller, J.: Diachronous Variscan tectonothermal activity in the NW Iberian Massif: Evidence from 40Ar/39Ar dating of regional fabrics, Tectonophysics, 277, 307–337, https://doi.org/10.1016/S0040-1951(97)00035-8, 1997.

Dallmeyer, R. D., Ribeiro, A., and Marques, F.: Polyphase Variscan emplacement of exotic terranes (Morais and Bragança Massifs) onto Iberian successions: Evidence from 40Ar/39Ar mineral ages, Lithos, 27, 133–144, https://doi.org/10.1016/0024-4937(91)90025-G, 1991.

de Pablo Maciá, J. G. and Martínez Catalán, J. R.: Estructura, petrología y evolución de la región de Sobrado de los Monjes (La Coruña), Cad. Lab. Xeol. Laxe., 7, 103–124, 1984.

DeWolf, C. P., Belshaw, N., and O'Nions, R. K.: A metamorphic history from micron-scale 207Pb/206Pb chronometry of Archean monazite, Earth Planet. Sc. Lett., 120, 207–220, 1993.

Dias da Silva, I., Valverde-Vaquero, P., González-Clavijo, E., Díez-Montes, A., and y Martínez Catalán, J. R.: Structural and stratigraphical significance of U–Pb ages from the Mora and Saldanha volcanic complexes (NE Portugal, Iberian Variscides), in: Schulmann, K., Martínez Catalán, J. R., Lardeaux, J. M., Janousek, V., and Oggiano, G.: The Variscan Orogeny: Extent, Timescale, the Formation of the European Crust, Geological Society, London, Special Publications, 405, https://doi.org/10.1144/SP405.3, 2014.

Díaz García, F., Martínez Catalán, J. R., Arenas, R., and González Cuadra, P.: Structural and kinematic analysis of the Corredoiras detachment: evidence for early Variscan synconvergent extension in the Ordenes Complex, NW Spain, Int. J. Earth Sci., 88, 337–351, 1999.

Díez Fernández, R., Catalán, J. R. M., Gerdes, A., Abati, J., Arenas, R., and Fernández-Suárez, J.: U–Pb ages of detrital zircons from the Basal allochthonous units of NW Iberia: Provenance and paleoposition on the northern margin of Gondwana during the Neoproterozoic and Paleozoic. Gondwana Res., 18, 385–399, https://doi.org/10.1016/j.gr.2009.12.006, 2010.

Díez Fernández, R., Martínez Catalán, J. R., Arenas, R., Abati, J., Gerdes, A., and Fernández-Suárez, J.: U–Pb detrital zircon analysis of the lower allochthon of NW Iberia: age constraints, provenance and links with the Variscan mobile belt and Gondwanan cratons, J. Geol. Soc. London, 169, 655–665, https://doi.org/10.1144/jgs2011-146, 2012.

Egal, E., Thiéblemont, D., Lahondère, D., Guerrot, C., Costea, C. A., Iliescu, D., Delor, C., Goujou, J. C., Lafon, J. M., Tegyey, M., Diaby, S., and Kolié, P.: Late Eburnean granitization and tectonics along the western and northwestern margin of the

Archean Kenema-Man domain (Guinea, West African Craton), Precambrian Res., 117, 57–84, https://doi.org/10.1016/S0301-9268(02)00060-8, 2002.

Ennih, N. and Liegeois, J.-P.: The boundaries of the West African craton, with special reference to the basement of the Moroccan metacratonic Anti-Atlas belt, The Boundaries of the West African Craton, 1–17, https://doi.org/10.1144/SP297.1, 2008.

Farias, P., Gallastegui, G., González Lodeiro, F., Marquínez, J., Martín Parra, L. M., Martínez Catalán, J. R., de Pablo Maciá, J. G., and Rodríguez Fernández, L. R.: Aportaciones al conocimiento de la litoestratigrafía y estructura de Galicia Central. Memórias da Faculdade de Ciências, Universidade do Porto 1, 411–431, 1987.

Fernández-Suárez, J., Arenas, R., Abiati, J., Martinez Catalán, J. R., Whitehouse, M., and Jeffries, T.: U-Pb chronometry of polymetamorphic high-pressure granulites: An example from the allochthonous terranes of the NW Iberian Variscan belt, Geol. Soc. Am. Mem., 200, 469–488, https://doi.org/10.1130/2007.1200(24), 2007.

Fernández-Suárez, J., Corfu, F., Arenas, R., Marcos, A., Martínez Catalán, J. R., Díaz García, F., Abati, J., and Fernández, F. J.: U-Pb evidence for a polyorogenic evolution of the HP-HT units of the NW Iberian Massif, Contrib. Mineral. Petr., 143, 236–253, https://doi.org/10.1007/s00410-001-0337-2, 2002.

Fernández-Suárez, J., Garcia, F. D., Jeffries, T. E., and Arenas, R.: Constraints on the provenance of the uppermost allochthonous terrane of the NW Iberian Massif: inferences from detrital zircon U-Pb ages, Terra Nova, 15, 138–144, https://doi.org/10.1046/j.1365-3121.2003.00479.x, 2003.

Franz, G. and Spear, F. S.: Aluminous Titanite (sphene) from the Eclogite Zone, south-central Tauern window, Austria, Chem. Geol., 50, 33–46, https://doi.org/10.1016/0009-2541(85)90110-X, 1985.

Frost, B. R., Chamberlain, K. R., and Schumacher, J.C.: Sphene (titanite): phase relations and role as a geochronometer, Chem. Geol., 172, 131–148, https://doi.org/10.1016/S0009-2541(00)00240-0, 2000.

Fuenlabrada, J., Arenas, R., Sánchez-Martínez, S., Díaz García, F., and Castiñeiras, P.: A peri-Gondwanan arc in NW Iberia I: Isotopic and geochemical constraints on the origin of the arc-A sedimentary approach, Gondwana Res., 17, 338–351, https://doi.org/10.1016/j.gr.2009.09.007, 2010.

Gagnevin, D. and Daly, J. S.: Zircon texture and chemical composition as a guide to magmatic processes and mixing in a granitic environment and coeval volcanic system, https://doi.org/10.1007/s00410-009-0443-0, 2010.

Gómez Barreiro, J., Wijbrans, J. R., Castiñeiras, P., Martínez Catalán, J. R., Arenas, R., Díaz García, F., and Abati, J.: $^{40}Ar/^{39}Ar$ laserprobe dating of mylonitic fabrics in a polyorogenic terrane of NW Iberia, J. Geol. Soc. London, 163, 61–73, https://doi.org/10.1144/0016-764905-012, 2006.

Gómez-Barreiro, J., Martínez Catalán, J. R., Arenas, R., Castiñeiras, P., Abati, J., Díaz García, F., and Wijbrans, J. R.: Tectonic evolution of the upper allochthon of the Órdenes complex (northwestern Iberian Massif): Structural constraints to a polyorogenic peri-Gondwanan terrane, Geol. S. Am., 423, 315–332, https://doi.org/10.1130/2007.2423(15), 2007.

Goncalves, P., Williams, M. L., and Jercinovic, M. J.: Electron-microprobe age mapping of monazite, Am. Mineral., 90, 578–585, https://doi.org/10.2138/am.2005.1399, 2005.

Grimes, C. B., Wooden, J. L., Cheadle, M. J., and John, B. E.: “Fingerprinting” tectono-magmatic provenance using trace elements in igneous zircon, Contrib. Mineral. Petr., 170, 1–26, https://doi.org/10.1007/s00410-015-1199-3, 2015.

Hacker, B. R., Kylander-clark, A. R. C., Holder, R., Andersen, T. B., Peterman, E. M., Walsh, E. O., and Munnikhuis, J. K.: Monazite response to ultrahigh-pressure subduction from U-Pb dating by laser ablation split stream, Chem. Geol., 409, 28–41, https://doi.org/10.1016/j.chemgeo.2015.05.008, 2015.

Hanchar, J. M. and Van Westrenen, W.: Rare earth element behavior in zircon-melt systems, Elements, 3, 37–42, https://doi.org/10.2113/gselements.3.1.37, 2007.

Harlov, D., Tropper, P., Seifert, W., Nijland, T., and Förster, H.-J.: Formation of Al-rich titanite ($CaTiSiO_4O$ – $CaAlSiO_4OH$) reaction rims on ilmenite in metamorphic rocks as a function of fH_2O and fO_2, Lithos, 88, 72–84, https://doi.org/10.1016/j.lithos.2005.08.005, 2006.

Hawkins, D. P. and Bowring, S. A.: U-Pb systematics of monazite and xenotime?: case studies from the Paleoproterozoic of the Grand Canyon, Arizona, 87–103, 1997.

Hermann, J. and Rubatto, D.: Relating zircon and monazite domains to garnet growth zones?: Age and duration of granulite facies metamorphism in the Val Malenco lower crust, Journal of Metamorphic, 21, 833–852, https://doi.org/10.1046/j.1525-1314.2003.00484.x, 2003.

Hokada, T. and Harley, S. L.: Zircon growth in UHT leucosome: constraints from zircon-garnet rare earth elements (REE) relations in Napier Complex, East Antarctica, J. Miner. Petrol. Sci., 99, 180–190, https://doi.org/10.2465/jmps.99.180, 2004.

Holder, R. M., Hacker, B. R., Kylander-Clark, A. R. C., and Cottle, J. M.: Monazite trace-element and isotopic signatures of (ultra) high-pressure metamorphism?: Examples from the Western Gneiss Region, Norway, Chem. Geol., 409, 99–111, https://doi.org/10.1016/j.chemgeo.2015.04.021, 2015.

Horstwood, M. S. A., Foster, G. L., Parrish, R. R., Noble, S. R., and Nowell, G. M.: Common-Pb corrected in situ U–Pb accessory mineral geochronology by LA-MC-ICP-MS, J. Anal. At. Spectrom, 18, 837–846, https://doi.org/10.1039/b304365g, 2003.

Hoskin, P. W. O.: Trace-element composition of hydrothermal zircon and the alteration of Hadean zircon from the Jack Hills, Australia, Geochim. Comochim. Ac., 69, 637–648, https://doi.org/10.1016/j.gca.2004.07.006, 2005.

Hoskin, P. W. O. and Ireland, T. R.: Rare earth element chemistry of zircon and its use as a provenance indicator, Geology, 28, 627–630, https://doi.org/10.1130/0091-7613(2000)28<627:REECOZ>2.0.CO;2, 2000.

Hoskin, P. W. O. and Schaltegger, U.: The Composition of Zircon and Igneous and Metamorphic Petrogenesis, in: Hanchar, J. M. and Hoskin, P. W. O., Zircon, Reviews in Mineralogy and Geochemistry, Mineralogical Society of America, 27–62, 2003.

Jackson, S. E., Pearson, N. J., Griffin, W. L., and Belousova, E. A.: The application of laser ablation-inductively coupled plasma-mass spectrometry to in situ U-Pb zircon geochronology, Chem. Geol., 211, 47–69, https://doi.org/10.1016/j.chemgeo.2004.06.017, 2004.

Ji, S. and Martignole, J.: Ductility of garnet as an indicator of extremely high temperature deformation, J. Struct. Geol., 16, 985–996, 1994.

Kleinschrodt, R. and Duyster, J.: HT-deformation of garnet: an EBSD study on granulites from Sri Lanka, India and the Ivrea Zone, J. Struct. Geol., 24, 1829–1844, 2002.

Kohn, M. J. and Malloy, M. A.: Formation of monazite via prograde metamorphic reactions among common silicates?: Implications for age determinations, Geochim. Comochim. Ac., 68, 101–113, https://doi.org/10.1016/S0016-7037(03)00258-8, 2004.

Košler, J., Tubrett, M. N., and Sylvester, P. J.: Application of laser ablation ICP-MS to U-Th-Pb dating of monazite, Geostandard Newslett., 25, 375–386, https://doi.org/10.1111/j.1751-908X.2001.tb00612.x, 2001.

Kuijper, R. P.: U-Pb systematic and petrogenetic evolution of infracrustal rocks in the Paleozoic basement of Western Galicia, NW Iberia, WO Laboratory of Isotope Geology, Amsterdam, 1979.

Kylander-Clark, A. R. C., Hacker, B. R., and Cottle, J. M.: Laser-ablation split-stream ICP petrochronology. Chem. Geol., 345, 99–112, https://doi.org/10.1016/j.chemgeo.2013.02.019, 2013.

Lesnov, F. P.: Consistent patterns of rare earth element distribution in accessory minerals from rocks of mafic-ultramafic complexes, Cent. Eur. J. Geosci., 5, 112–173, https://doi.org/10.2478/s13533-012-0121-z, 2013.

Ludwig, K. R.: On the Treatment of Concordant Uranium-Lead Ages, Geochim. Comochim. Ac., 62, 665–676, https://doi.org/10.1016/S0016-7037(98)00059-3, 1998.

Ludwig, K. R.: User's Manual for ISOPLOT version 3.75, A Geochronological Toolkit for Microsoft Excel, Berkeley Geochronology Center, 2012.

Ludwig, K. R. and Mundil, R.: Extracting reliable U–Pb ages and errors from complex populations of zircons from Phanerozoic tuffs, Geochim. Comochim. Ac., 66, 463, 2002.

Martínez Catalán, J. R., Arenas, R., Díaz García, F., and Abati, J.: Allochthonous Units in the Variscan Belt of NW Iberia: Terranes and Accretionary History, in: Basement Tectonics 13, edited by: Sinha, A. K., Proceedings of the Thirteenth International Conference on Basement Tectonics Held in Blacksburg, Virginia, USA, June 1997, Springer Netherlands, Dordrecht, 65–84, https://doi.org/10.1007/978-94-011-4800-9_5, 1999.

Martínez Catalán, J. R., Fernández-Suárez, J., Jenner, G. A., Belousova, E., and Díez Montes, A.: Provenance constraints from detrital zircon U–Pb ages in the NW Iberian Massif: implications for Paleozoic plate configuration and Variscan evolution, J. Geol. Soc. London, 161, 461–473, https://doi.org/10.1144/0016-764903-054, 2004,

Martínez Catalán, J. R., Arenas, R., Abati, J., Sánchez Martínez, S., Díaz García, F., Fernaández Suaárez, J., González Cuadra, P., Castiñeiras, P., Gómez Barreiro, J., Díez Montes, A., González Clavijo, E., Rubio Pascual, F. J., Andonaegui, P., Jeffries, T. E., Alcock, J. E., Diíez Fernández, R., and López Carmona, A.: A rootless suture and the loss of the roots of a mountain chain: The Variscan belt of NW Iberia, C. R. Geosci., 341, 114–126, https://doi.org/10.1016/j.crte.2008.11.004, 2009.

Martínez Catalán, J. R.: Are the oroclines of the Variscan belt related to late Variscan strike-slip tectonics?, Terra Nova, 23, 241–247, https://doi.org/10.1111/j.1365-3121.2011.01005.x, 2011.

Martínez Catalán, J. R.: The Central Iberian arc, an orocline centered in the Iberian Massif and some implications for the Variscan belt, Int. J. Earth Sci., 101, 1299–1314, https://doi.org/10.1007/s00531-011-0715-6, 2012.

McDonough, W. F. and Sun, S. S.: The composition of the Earth, Chem. Geol., 120, 223–253, https://doi.org/10.1016/0009-2541(94)00140-4, 1995.

Möller, A., O'Brien, P. J., Kennedy, A., and Kröner, A.: Polyphase zircon in ultrahigh-temperature granulites (Rogaland, SW Norway): Constraints for Pb diffusion in zircon, J. Meetamorph. Geol., 20, 727–740, https://doi.org/10.1046/j.1525-1314.2002.00400.x, 2002.

Mottram, C. M., Warren, C. J., Regis, D., Roberts, N. M. W., Harris, N. B. W., Argles, T. W., and Parrish, R. R.: Developing an inverted barrovian sequence; insights from monazite petrochronology, Earth Planet. Sc. Lett., 403, 418–431, https://doi.org/10.1016/j.epsl.2014.07.006, 2014.

Mulrooney, D. and Rivers, T.: Redistribution of the rare-earth elements among coexisting minerals in metamafic rocks across the epidote-out isograd: An example from the St. Anthony Complex, northern Newfoundland, Canada, Can. Mineral., 43, 263–294, https://doi.org/10.2113/gscanmin.43.1.263, 2005.

Nasdala, L., Zhang, M., Kempe, U., Panczer, G., Gaft, M., Andrut, M., and Plötze, M.: Spectroscopic methods applied to zircon, in: Zircon. Reviews in Mineralogy and Geochemistry, edited by: Hanchar, J. M. and Hoskin, P. W. O., Mineral. Soc. Am., 427–467, 2003.

Ordóñez Casado, B.: Geochronological studies of the pre-Mesozoic basement of the Iberian Massif?: the Ossa Morena zone and the Allochthonous Complexes within the Central Iberian zone, PhD thesis, Swiss Federal Institute of Technology, Zürich, Switzerland, 235 pp., https://doi.org/10.3929/ethz-a-002017279, 1998.

Ordóñez Casado, B., Gebauer, D., Schäfer, H. J., Ibarguchi, J. I. G., and Peucat, J. J.: A single Devonian subduction event for the HP/HT metamorphism of the Cabo Ortegal complex within the Iberian Massif, Tectonophysics, 332, 359–385, https://doi.org/10.1016/S0040-1951(00)00210-9, 2001.

Palin, R. M., Searle, M. P., Waters, D. J., Parrish, R. R., Roberts, N. M. W., Horstwood, M. S. A., Yeh, M. W., Chung, S. L., and Anh, T. T.: A geochronological and petrological study of anatectic paragneiss and associated granite dykes from the Day Nui Con Voi metamorphic core complex, North Vietnam: Constraints on the timing of metamorphism within the Red River shear zone, J. Meetamorph. Geol., 31, 359–387, https://doi.org/10.1111/jmg.12025, 2013.

Passchier, C. W. and Trouw, R. A. J.: Microtectonics, Springer Science & Business Media, Berlin, Heidelberg, 2005.

Paton, C., Hellstrom, J., Paul, B., Woodhead, J., and Hergt, J.: Iolite: Freeware for the visualisation and processing of mass spectrometric data, J. Anal. Atom. Spectrom., 26, 2508, https://doi.org/10.1039/c1ja10172b, 2011.

Peters, T. J., Ayers, J. C., Gao, S., and Liu, X. M.: The origin and response of zircon in eclogite to metamorphism during the multi-stage evolution of the Huwan Shear Zone, China: Insights from Lu-Hf and U-Pb isotopic and trace element geochemistry, Gondwana Res., 23, 726–747, https://doi.org/10.1016/j.gr.2012.05.008, 2013.

Peucat, J. J., Bernard Griffiths, J., Ibarguchi, J. I. G., Dallmeyer, R. D., Menot, R. P., Cornichet, J., and Ponce de León, M. I.:

Geochemical and Geochronological Cross-Section of the Deep Variscan Crust – the Cabo-Ortegal High-Pressure Nappe (Northwestern Spain), Tectonophysics, 177, 263–292, 1990.

Peucat, J. J., Capdevila, R., Drareni, A., Mahdjoub, Y., and Kahoui, M.: The Eglab massif in the West African Craton (Algeria), an original segment of the Eburnean orogenic belt: Petrology, geochemistry and geochronology, Precambrian Res., 136, 309–352, https://doi.org/10.1016/j.precamres.2004.12.002, 2005.

Potrel, A., Peucat, J. J., and Fanning, C. M.: Archean crustal evolution of the West African Craton: example of the Amsaga Area (Reguibat Rise). U-Pb and Sm-Nd evidence for crustal growth and recycling, Precambrian Res., 90, 107–117, https://doi.org/10.1016/S0301-9268(98)00044-8, 1998.

Ribeiro, A., Pereira, E., and Dias, R.: Central-Iberian Zone. Allochthonous Sequences. Structure in the Northwest of the Iberian Peninsula, in: Pre-Mesozoic Geology of Iberia, edited by: Dallmeyer, R. D. and y Martínez García, E., Springer, Berlin, 220–236, 1990.

Rubatto, D.: Zircon trace element geochemistry?: distribution coefficients and the link between U-Pb ages and metamorphism Zircon trace element geochemistry?: partitioning with garnet and the link between U-Pb ages and metamorphism, Chem. Geol., 184, 123–138, 2002.

Rubatto, D., and Hermann, J.: Exhumation as fast as subduction?, Geology, 29, 3–6, 2001.

Rubatto, D., Hermann, R. G., and Buick, I. S.: Temperature and Bulk Composition Control on the Growth of Monazite and Zircon During Low-pressure Anatexis (Mount Stafford , Central Australia), J. Petrol., 47, 1973–1996, https://doi.org/10.1093/petrology/egl033, 2006.

Rubatto, D., Hermann, J., Berger, A., and Engi, M.: Protracted fluid-induced melting during Barrovian metamorphism in the Central Alps, Contrib. Mineral. Petr., 158, 703–722, https://doi.org/10.1007/s00410-009-0406-5, 2009.

Rubatto, D., Chakraborty, S., and Dasgupta, S.: Timescales of crustal melting in the Higher Himalayan Crystallines (Sikkim, Eastern Himalaya) inferred from trace element-constrained monazite and zircon chronology, Contrib. Mineral. Petr., 165, 349–372, https://doi.org/10.1007/s00410-012-0812-y, 2013.

Santos Zalduegui, J. F., Schärer, U., and Gil Ibarguchi, J. I.: Isotope constraints on the age and origin of magmatism and metamorphism in the Malpica-Tuy allochthon, Galicia, NW Spain. Chem. Geol., 121, 91–103, https://doi.org/10.1016/0009-2541(94)00123-P, 1995.

Santos Zalduegui, J. F., Schärer, U., Gil Ibarguchi, J. I., and Girardeau, J.: Origin and evolution of the Paleozoic Cabo Ortegal ultramafic-mafic complex (NW Spain): U-Pb, Rb-Sr and Pb-Pb isotope data, Chem. Geol., 129, 281–304, https://doi.org/10.1016/0009-2541(95)00144-1, 1996.

Santos Zalduegui, J. F., Schärer, U., Gil Ibarguchi, J. I., and Girardeau, J.: Genesis of Pyroxenite-rich Peridotite at Cabo Ortegal (NW Spain): Geochemical and Pb-Sr-Nd Isotope Data, J. Petrol., 43, 17–43, https://doi.org/10.1093/petrology/43.1.17, 2002.

Schofield, D. I., Horstwood, M. S. A., Pitfield, P. E. J., Gillespie, M., Darbyshire, F., O'Connor, E. A., and Abdouloye, T. B.: U-Pb dating and Sm-Nd isotopic analysis of granitic rocks from the Tiris Complex: New constaints on key events in the evolution of the Reguibat Shield, Mauritania, Precambrian Res., 204–205, 1–11, https://doi.org/10.1016/j.precamres.2011.12.008, 2012.

Spear, F. S.: An experimental study of hornblende stability and compositional variability in amphibolite, Am. J. Sci., 281, 697–734, https://doi.org/10.2475/ajs.281.6.697, 1981.

Spear, F. S. and Pyle, J. M.: Apatite , Monazite , and Xenotime in Metamorphic Rocks, in: Phosphates: Geochemical, Geobiological, and Materials Importance edited by: Kohn, M. J., Rakovan, J., and Hughes, J. M., Rev. Mineral. Geochem., 48, 293–335, https://doi.org/10.2138/rmg.2002.48.7, 2002.

Spencer, K. J., Hacker, B. R., Kylander-Clark, A. R. C., Andersen, T. B., Cottle, J. M., Stearns, M. A., Poletti, J. E., and Seward, G. G. E.: Campaign-style titanite U – Pb dating by laser-ablation ICP?: Implications for crustal flow, phase transformations and titanite closure, Chem. Geol., 341, 84–101, https://doi.org/10.1016/j.chemgeo.2012.11.012, 2013.

Stearns, M. A., Hacker, B. R., Ratschbacjer, L., Rutte, D., and Kylander-Clark, A. R. C.: Titanite petrochronology of the Pamir gneiss domes: Implications for middle to deep crust exhumation and titanite closure to Pb and Zr diffusion, Tectonics, 34, 784–802, https://doi.org/10.1002/2014TC003774, 2015.

Stearns, M. A., Cottle, J. M., Hacker, B. R., and Kylander-Clark, A. R. C.: Extracting thermal histories from the near-rim zoning in titanite using coupled U-Pb and trace-element depth profiles by single-shot laser-ablation split stream (SS-LASS) ICP-MS, Chem. Geol., 422, 13–24, https://doi.org/10.1016/j.chemgeo.2015.12.011, 2016.

Stipska, P., Powell, R., Hacker, B. R., and Holder, R.: Uncoupled U/Pb and REE response in zircon during the transformation of eclogite to mafic and intermediate granulite (Blansk y les, Bohemian Massif), J. Metamorph. Geol., 34, 551–572, https://doi.org/10.1111/jmg.12193, 2016.

Storey, C. D., Smith, M. P., and Jeffries, T. E.: In situ LA-ICP-MS U – Pb dating of metavolcanics of Norrbotten, Sweden?: Records of extended geological histories in complex titanite grains, Chem. Geol., 240, 163–181, https://doi.org/10.1016/j.chemgeo.2007.02.004, 2007.

Stübner, K., Grujic, D., Parrish, R. R., Roberts, N. M. W., Kronz, A., Wooden, J., and Ahmad, T.: Lithos Monazite geochronology unravels the timing of crustal thickening in NW Himalaya, Lithos, 210–211, 111–128, https://doi.org/10.1016/j.lithos.2014.09.024, 2014.

Tera, F. and Wasserburg, G. J.: U-Th-Pb systematics in three Apollo 14 basalts and the problem of initial Pb in lunar rocks, Earth Planet. Sc. Lett., 14, 281–304, https://doi.org/10.1016/0012-821X(72)90128-8, 1972.

Terry, M. P. and Hamilton, M. A.: Monazite geochronology of UHP and HP metamorphism, deformation, and exhumation, Nordoyane, Western Gneiss Region, Norway, American Mineralogist, 85, 1651–1664, https://doi.org/10.2138/am-2000-11-1208, 2000.

Tomascak, P. B., Krogstad, E. J., and Walker, R. J.: U-Pb Monazite Geochronology of Granitic Rocks from Maine: Implications for Late Paleozoic Tectonics in the Northern Appalachians, J. Geol., 104, 185–195, 1996.

Verts, L. A. and Frost, C. D.: U-Pb sphene dating of metamorphism?: the importance of sphene growth in the contact aureole of the Red Mountain pluton, Laramie Mountains, Wyoming, Contrib. Mineral. Petr., 125, 186–199, https://doi.org/10.1007/s004100050215, 1996.

Watson, E. B. and Yan L.: A simple model for sector zoning in slowly grown crystals: implications for growth rate and lattice diffusion, with emphasis on accessory minerals in crustal rocks, Am. Mineral., 80, 1179–1187, 1995.

Whitehouse, M. J. and Platt, .J. P.: Dating high-grade metamorphism – constraints from rare-earth elements in zircon and garnet, Contrib. Mineral. Petr., 145, 61–74, https://doi.org/10.1007/s00410-002-0432-z, 2003.

Whitney, D. L. and Evans, B. W.: Abbreviations for names of rock-forming minerals, Am. Mineral., 95, 185–187, https://doi.org/10.2138/am.2010.3371, 2010.

Wieldenbeck, M., Allé, P., Corfú, F., Griffin, W. L., Meier, M., Oberli, F., von Quadt, A., Roddick, J. C., and Spiegel, W.: Three Natural Zircon Standards for U-Th-Pb, Lu-Hf, Trace Element and REE Analyses, Geostandard Newslett., 19, 1–23, https://doi.org/10.1111/j.1751-908X.1995.tb00147.x, 1995.

Williams, M. L., Jercinovic, M. J., and Hetherington, C. J.: Microprobe Monazite Geochronology: Understanding Geologic Processes by Integrating Composition and Chronology, Annu. Rev. Earth Pl. Sc., 35, 137–175, https://doi.org/10.1146/annurev.earth.35.031306.140228, 2007.

Zeck, H. P., Wingate, M. T. D., Pooley, G. D., Ugidos, and J. M.: A Sequence of Pan-African and Hercynian Events Recorded in Zircons from an Orthogneiss from the Hercynian Belt of Western Central Iberia – an Ion Microprobe U-Pb Study, Journal of Petrology, 45, 1613–1629, https://doi.org/10.1093/petrology/egh026, 2004.

Zeringue, J., Bowring, J. F., McLean, N. M., and Pastor, F.: Building Interactive Visualizations for Geochronological Data, AGU Fall Meeting Abstracts, 2014.

Zhu, X. K., O'Nions, R. K., Belshaw, N. S., and Gibb, A. J.: Significance of in situ SIMS chronometry of zoned monazite from the Lewisian granulites, northwest Scotland. Chem. Geol., 5, 35–53, https://doi.org/10.1016/S0009-2541(96)00103-9, 1997.